UNIVERSIDAD DE CHILE
FACULTAD DE CIENCIAS FÍSICAS Y MATEMÁTICAS
DEPARTAMENTO DE FÍSICA

DYNAMICS OF CONFINED MICROSWIMMERS INSIDE A DROPLET: FROM MICROACTIVITY TO MACROMOVEMENT

TESIS PARA OPTAR AL GRADO DE
DOCTOR EN CIENCIAS, MENCIÓN FÍSICA

GABRIEL PATRICIO RAMOS PERONI

PROFESORES GUÍA:
MARÍA LUISA CORDERO GARAYAR
RODRIGO SOTO BERTRÁN

MIEMBROS DE LA COMISIÓN:
VERÓNICA MARCONI
NICOLÁS MUJICA FERNÁNDEZ

SANTIAGO DE CHILE
2020

RESUMEN DE LA TESIS PARA OPTAR AL GRADO DE
DOCTOR EN CIENCIAS, MENCIÓN FÍSICA
POR: GABRIEL PATRICIO RAMOS PERONI
FECHA: 2020
PROF. GUÍA: MARÍA LUISA CORDERO GARAYAR RODRIGO SOTO BERTRÁN

En esta tesis investigamos tres experimentos en los que confinamos suspensiones bacterianas al interior de microgotas. El objetivo de estos experimentos es entender cómo la microactividad a escala local, cuando las bacterias se organizan colectivamente, es capaz de crear macromovimientos a escalas del tamaño de la gota confinante, la cual es cerca de 100 veces el tamaño de una bacteria. En otras palabras, cómo podemos extraer trabajo útil a partir de suspensiones confinadas.

Primero, confinamos una suspensión de *Escherichia coli* dentro de gotas en una emulsión agua-aceite, creando una gota propulsada por bacterias. Mostramos que las gotas realizan un movimiento aleatorio persistente, con tiempo de persistencia $\tau \sim 0.3\,\mathrm{s}$, coeficiente de difusión a tiempos largos $D \sim 0.5\,\mu\mathrm{m}^2/\mathrm{s}$, y rapidez instantánea promedio $V \sim 1.5\,\mu\mathrm{m/s}$ a la máxima concentración bacteriana estudiada. Variamos el radio de la gota y la concentración bacteriana, mostrando que el tiempo de persistencia, coeficiente de difusión y rapidez promedio aumentan con la concentración de bacterias, pero son independientes del radio de la gota. Por último, demostramos que la velocidad promedio de las bacterias en el fondo de la gota, el cual está separado del sustrato de vidrio por una delgada película de lubricación de aceite, es antiparalela a la velocidad instantánea de la gota. Esto sugiere que el mecanismo de desplazamiento es una rotación con deslizamiento de la gota sobre el sustrato, causado por el movimiento colectivo de las bacterias. Nuestros resultados muestran que organismos microscópicos pueden trasferir energía mecánica útil a su entorno, abriendo la posibilidad de generar motores mesoscópicos compuestos de micronadadores.

En un segundo experimento, mostramos que bajo la aplicación de un campo magnético constante, bacterias magnetotácticas confinadas en una emulsión agua-aceite se autoensamblan en un motor rotatorio ejerciendo un torque sobre la fase oleosa externa. Un movimiento colectivo en la forma de un vórtice de gran escala, reversible al invertir la dirección del campo magnético, se genera al interior de la gota con una vorticidad perpendicular al campo magnético. Estudiamos este movimiento colectivo a diferentes concentraciones de bacterias, campos magnéticos y radios de gota, revelando la formación de dos áreas generadoras de torque cerca de la interfaz. Caracterizamos cuantitativamente la energía mecánica extraíble de este nuevo motor biológico autoensamblado.

Finalmente, estudiamos una suspensión bacteriana de *E.coli* confinada en una doble emulsión, donde una gota de aceite queda atrapada al interior de una emulsión agua-aceite. Mostramos que la gota interior de aceite realiza un movimiento aleatorio persistente en el plano horizontal con un tiempo de persistencia de $\tau \sim 0.3\,\mathrm{s}$. El coeficiente de difusión en el plano horizonal depende inversamente del radio de la gota interna, y lo comparamos con el coeficiente de difusión termal. Con esto calculamos una temperatura activa, obteniendo un valor de $2.7 \times 10^4\mathrm{K}$, dos órdenes de magnitud mayor que la temperatura ambiente, consistente con el experimento de gotas propulsadas por bacterias y trabajos previos. Estudiamos también el plano vertical, mostrando que el coeficiente de difusión en este plano es menor que en el horizontal, debido al atrapamiento geométrico.

THESIS ABSTRACT
BY: GABRIEL PATRICIO RAMOS PERONI
DATE: 2020
SUPERVISOR: MARÍA LUISA CORDERO GARAYAR RODRIGO SOTO BERTRÁN

In this thesis we investigate three experiments where bacterial suspensions are encapsulated in droplets. The aim of these experiments is to understand how the microactivity at the local scale, when bacteria organize collectively, can create a macromovement at the containing droplet scale, which is about 100 times the size of a bacterium. In other words, how we can extract useful work from these encapsulated bacterial suspensions.

First, we confine a dense suspension of motile *Escherichia coli* inside a spherical droplet in a water-in-oil emulsion, creating a "bacterially" propelled droplet. We show that droplets move in a persistent random walk, with a persistence time $\tau \sim 0.3\,\mathrm{s}$, a long-time diffusion coefficient $D \sim 0.5\,\mu\mathrm{m}^2/\mathrm{s}$, and an average instantaneous speed $V \sim 1.5\,\mu\mathrm{m/s}$ when the bacterial suspension is at the maximum studied concentration. Several droplets are analyzed, varying the drop radius and bacterial concentration. We show that the persistence time, diffusion coefficient and average speed increase with the bacterial concentration inside the drop, but are largely independent of the droplet size. By measuring the turbulent-like motion of the bacteria inside the drop, we demonstrate that the mean velocity of the bacteria near the bottom of the drop, which is separated from a glass substrate by a thin lubrication oil film, is antiparallel to the instantaneous velocity of the drop. This suggests that the driving mechanism is a slippery rolling of the drop over the substrate, caused by the collective motion of the bacteria. Our results show that microscopic organisms can transfer useful mechanical energy to their confining environment, opening the way to the assembly of mesoscopic motors composed of microswimmers.

In a second experiment, we show that under the application of a constant magnetic field, motile magnetotactic bacteria confined in water-in-oil droplets self-assemble into a rotary motor exerting a torque on the external oil phase. A collective motion in the form of a large-scale vortex, reversable by inverting the field direction, builds-up in the droplet with a vorticity perpendicular to the magnetic field. We study this collective organization at different concentrations, magnetic fields and droplets radii and reveal the formation of two torque-generating areas close to the droplet interface. We characterize quantitatively the mechanical energy extractable from this new biological and self-assembled motor.

Finally, we study a bacterial suspension of *E.coli* encapsulated in a double emulsion, where an oil droplet gets trapped inside a water-in-oil emulsion. We show that the inner oil droplet performs a persistent random walk in the horizontal plane with a persistence time $\tau \sim 0.3\,\mathrm{s}$. The diffusion coefficient in the horizontal plane depends inversely on the inner droplet radius, and we compare it with the thermal diffusion coefficient. It allow us to compute an active temperature, which has a value of $2.7 \times 10^4\mathrm{K}$, two orders of magnitude larger than room temperature, consistent with the experiment of bacterially propelled droplets and previous works. The vertical plane was also studied, revealing that the diffusion coefficient in the vertical axis is smaller than in the horizontal axis, due to the geometric trapping.

Wüluwülungen. A los que luchan colectivamente, y mueven la historia.

Agradecimientos

A lo largo de todos estos años, es mucha gente la que quiero agradecer. Ha sido un periodo de crecimiento académico y personal. Al principio de esta tesis, no conocía nada de microbiología, agradezco a Juan Keymer y Janneke Noorlag por enseñarme y dar los primeros pasos en el mundo de las bacterias. También a la gente del CeBiB que fue buena onda, en especial Nancy que me ayudó cuando no tenía material, no sabía usar los equipos o no conocía algunos protocolos. Agradezco a Pablo, Camila, Vero y Nelson por los buenos recuerdos compartiendo en el tercer piso, y también por las risas y conversaciones en el laboratorio mientras hacíamos experimentos o alguna tontera. Gracias también a los postdocs, Pablo, Moniellen, Oscar y Andrea por la buena onda en los almuerzos en el laboratorio. Gracias José, Benjamín y Cristian por la simpatía y paciencia cuando les mostré los protocolos. Agradezco a Alvaro por alojarme todos estos años cuando necesitaba quedarme en Santiago, siempre con los brazos abiertos independientemente del día y la hora. Agradezco a Maria Luisa y Rodrigo por ser mis tutores y adentrarme más en el mundo de la investigación. Agradezco la confianza que depositaron en mí durante el doctorado para explorar y trabajar en el laboratorio, y agradezco las oportunidades que me dieron de poder ir a escuelas de verano y pasantías en el extranjero. Parte de los experimentos también los hice en el ESPCI en Francia, y fue super buena experencia para tomar más confianza conmigo mismo. Agradezco a Eric, Anke y Teresa por recibirme allá de forma acogedora. Agradezco a la gente con quien compartí, Benoit, Marcelo, Martyna, Jean, Gaspard y Jerome que hicieron que la pasantía en París fuera super agradable las dos veces que fui. Agradezco a mis padres y hermanos por apoyarme en mis decisiones y estar siempre orgullosos de mí, al igual que mi abuelita Edith que no alcanzó a ver el final de este proceso. Con todo el corazón agradezco a Céliane, por ser mi compañera y alentarme en todo momento. Gracias por embarcarte junto a mi en esta aventura y gracias por darme, junto a los niños, alegría todos los días. Este doctorado no podría haberse hecho sin la ayuda de ustedes, y por lo mismo, este doctorado no es solo mio, es un resultado colectivo.

Contents

List of Tables

List of Figures

Chapter 1

Introduction

1.1 What is active matter?

As a daily phenomenon, more than once we have asked ourselves about the collective motion performed by flocks of birds, groups of insects or even groups of people waking on the street. In all these cases, every *particle* moves independently, but for some reason the group moves together and sometimes performing complex patterns. How can physics help on the understanding and explanation of these phenomena? As we deal with a set of several particles, one way is by means of the statistical mechanics, one of the more successful tools in the study of big ensembles of particles, in equilibrium systems but also in slightly out of equilibrium systems. Going further, physicists have done great advances the last years with respect to systems completely out of equilibrium, observing complex patterns repeating at different scales, in living and synthetic systems where the key element is the injection and dissipation of energy. Particularly, when this energy injection and dissipation happens locally on each particle, common behavior have been observed in different systems independently on the mechanism of displacement of the particle and independently on the interaction between particles. Therefore, physicists coined the term *active matter* to refer to systems composed of a great number of particles, either living or synthetic, each one able to locally inject energy [1, 2]. This new research field has been of interest the last years, with an increase in the paper production related to this topic during the last decade [3]. Improvements on the theoretical and experimental aspects of the study of active matter have shown its enormous potential impact on fields like biophysics, medicine, etc.

One of the preferred systems to study active matter are the active suspensions. This type of suspensions are composed of autonomous microswimmers like bacteria, artificial self-propelled particles like active colloids (eg. Janus particles) or tubular micromotors. These microscopic systems offer the possibility of better controlling active matter properties [4], thanks to the improvements in microfluidics where accurate measurements can be done in small devices at low cost [5, 6, 7]. A classification of the active particles can be done depending on the form they organize. In general, there are three types in fluid phase [1]:

- **Polar active particles:** They have a head and a tail and are generally self-propelled

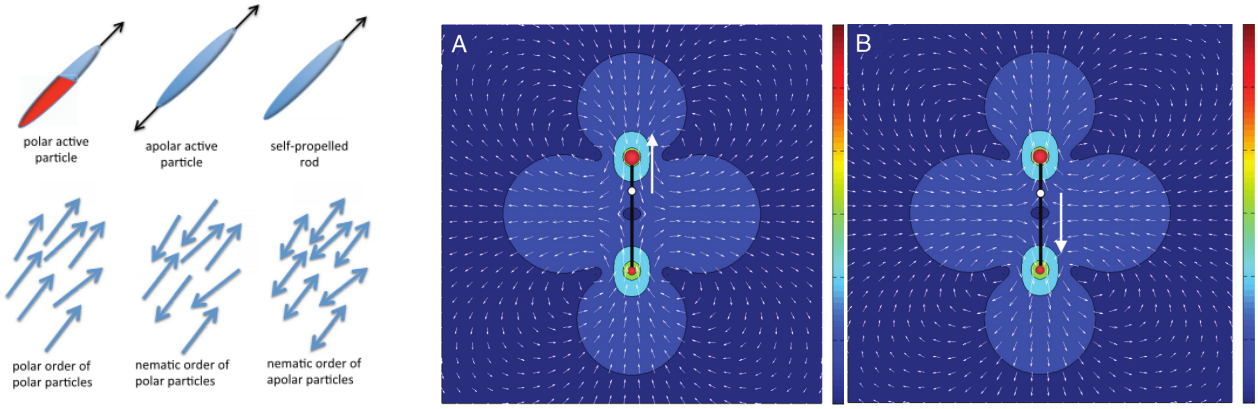

(a) (b)

Figure 1.1: (a) Schematic of the different types of active particles and orientationally ordered states (From Marchetti *et al.* [1]) (b) Flow patterns induced by the active forces on the fluid. Left: Puller swimmer. Right: Pusher swimmer. The color scale denote the amplitude of the flow from blue (weakest amplitude) to red (largest amplitude). The little arrows indicate the direction of the flow and the big white arrow is the direction of the self-propulsion velocity (From Baskaran and Marchetti [4]).

along their long axis moving in the head's direction(Fig.1.1a Top-left). They order in polar states (Fig.1.1a Bottom-left) or nematic states(Fig.1.1a Bottom-center).

- **Apolar active particles:** They are head-tail symmetric and move in any direction along their long axis.(Fig.1.1a Top-center). They order in nematic states.(Fig.1.1a Bottom- right)
- **Self-propelled rod** They are head-tail symmetric but each rod self propels in a specific direction along its long axis.(Fig.1.1a Top-right). In other words, self-propelled rods are polar in its movement, but symmetric in its geometry. For exclusively apolar interactions (such as steric effects), self-propelled rods order only in nematic states (Fig.1.1a Bottom-center).

As we previously mentioned, among the active suspensions we can consider different types of particles, but until nowadays, the most efficient microswimmers are build by Nature. This feature, together with their relatively easy manipulation and reproduction, have made bacterial suspensions popular to perform experiments.

1.2 Bacterial suspensions

Bacterial suspensions are collections of bacteria swimming in a fluid. Experiments with bacterial suspensions have been performed to study for example active diffusion [8], active viscosity[9] or collective motion[10]. In a bacterial suspension, each self-propelled bacterium can be modeled as force dipole, where its body exerts a force f on the fluid that is balanced by the rearward thrust $-f$ [11]. Depending on the dipole polarity, many biological microswimmers can be classified in two categories: pushers and pullers (Fig.1.1b). As an example,

bacteria such as *Escherichia coli* or *Bacillus subtilis* are classified as pushers, while algae such as *Chlamydomonas reinhardtii* are pullers. Numerical simulations on magnetotactic bacteria, suggest that they are puller swimmers as well[12], although no direct measurement of the flow around the bacterium has been performed in order to ensure this statement.

During this thesis, we have worked with bacterial suspensions using two types of bacteria, *Escherichia coli* and *Magnetospirillum gryphiswaldense* which we describe in the following.

1.2.1 *Escherichia coli*

The choice of using *Escherichia coli* (*E. coli*) comes from the fact that its biological and physical characteristics, such as its propulsion mechanism, are very well known. The *E. coli* has an ellipsoidal body shape with 1 µm diameter and 2 µm length (Fig.1.2a). This bacterium swims at low Reynolds number at an average speed of about 20 µm/s in aqueous media. The propulsion comes from the rotation of a helical bundle of 10 µm length flagella. When the bundle turns in a counter-clockwise direction, the bacterium is self propelled steadily forward and this receives the name of "run". If one or more flagella start to rotate clockwise, the bacterium changes direction, what is called a "tumble". The average duration of a run interval is 1 s, and the average tumble duration is 0.1 s[13]. This "run and tumble" process is typical for *E. coli* swimming in the bulk. Near boundaries, they tend to swim for a long time close to solid walls or fluid interfaces.

1.2.2 *Magnetospirillum gryphiswaldense*

This is a class of bacteria that can grow internally a microscopic magnet, called magnetosome, hence providing an external handle to drive their swimming orientation (Fig.1.2b) [15, 16].

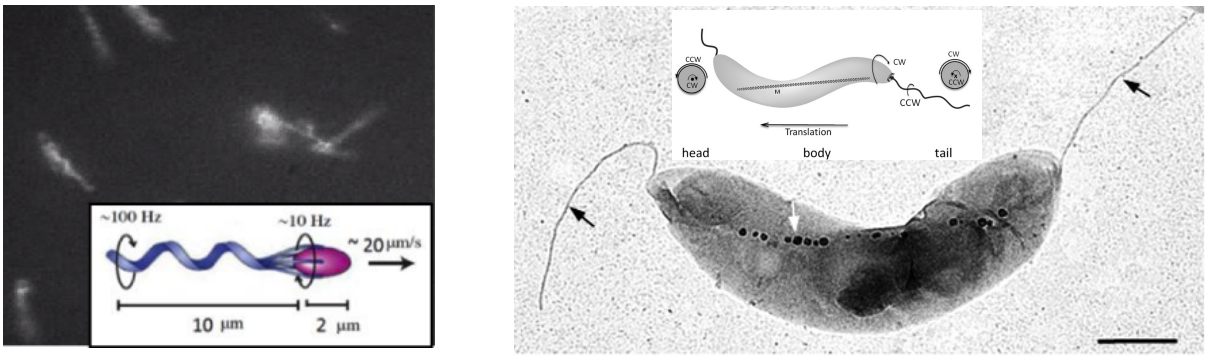

(a) (b)

Figure 1.2: (a) Fluorescence microscopy image of *Escherichia coli* (PMMH-ESCPI). Insert: Schematic representation of the cell body. (b) Electron micrograph of a magnetotactic bacterium, showing its two polar flagella (black arrows) and its magnetosome chain (white arrow). Scale bar 500 nm. Insert: Schematic representation of the cell body (From Murat *et al.*[14]).

The natural environment of these magnetotactic bacteria (MTB) is the bottom of lakes, where they follow the earth magnetic field in order to reach zones low in oxygen. As a source of nano-magnetic particles widely used in a medical context, MTB are micro-organisms of strong practical interest [17]. For example, the magnetic alignment, combined with a micro-aerotactic swimming response, qualifies such micro-swimmers as a promising vector for targeted drug therapy [18]. MTB have a helical body, of $\sim 5\,\mu m$ length, and swim with a speed V_0 ranging from 20 to $40\,\mu m/s$ and exhibit a magnetic moment $m \sim 10^{-16}\,J/T$. This bacterium has two flagella, one on each pole of the cell, the so-called amphitrichous bacterium. They have three motility behaviors, run, tumble and reversal. Experiments have shown that asymmetric rotation of the flagella (counterclockwise at the head and clockwise at the tail (Fig.1.2b)) enables cell runs whereas symmetric rotation triggers cell tumbling. In the case of cell reversals, they are caused by the simultaneous changes of rotation direction of both flagella [14]. The bacterial culture presents two types of population. When a constant magnetic field is applied on the suspension, roughly half of the population will swim persistently towards the (magnetic) north and the other half towards the south. The first population is called *north-seeker* (NS) and the other one *south-seeker* (SS).

1.3 Confined microswimmers

An interesting feature of microswimmers, is their hydrodynamic attraction to surfaces when they are confined, for example, in a microfluidic device [19, 20, 21, 22, 23]. It is observed that they swim exploring the bulk, but when they approach a surface, they get closer and swim along the surface, then they can leave this surface and be attracted eventually to the same or other surface [20].

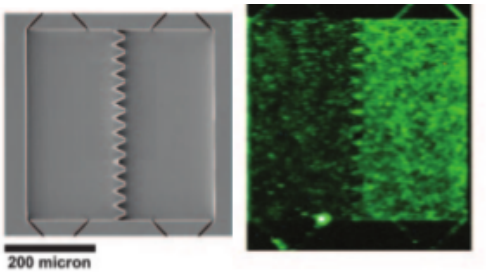

Figure 1.3: Microfluidic chamber used to concentrate bacteria. Left-Image shows the division at the center, with the funnel shaped walls, that guide bacteria. Right-Image shows the final stationary state of the system after 80 min. The initial condition was a homogeneous concentration of *E. coli* on both sides of the chamber (Modified from Galajda *et al.* [24]).

This behavior can be useful to increase the bacterial concentration in a specific region, as the system shown in Galajda et. al [24], where a microfluidic chamber divided in two with funnel shaped walls, concentrates a suspension of *E. coli* in one side of the device (Fig.1.3) profiting the attraction to surfaces. This kind of systems have useful applications in medicine, such as the case of guidance and trapping of human sperm cells for in vitro fertilization [25].

Another interesting behavior experimentally observed, is the circular movement performed by the *E. coli* when is attracted to the surface. Simulations have recovered this feature [21], establishing a phase diagram in which the bacterium can swim doing circles along the surface, stay at a fixed distance from the surface while performing the same circle, or leave the surface to the bulk, recovering the typical swimming behavior.

Most of the experiments have demonstrated this attraction and swimming along plane surfaces, but the last years, experiments and simulations have been carried out showing the

attraction to curved surfaces, either in concave walls [19, 20, 23] or convex walls [22, 23], observing in the latter that *E. coli* is attracted only if the radius of curvature of the surface is greater than 50 µm [22]. Curved confined active systems are ubiquitous in nature, such as confined bacteria in host cells [26] or the mammal corneal epithelium, that grows in a stationary vortex pattern [27]. In order to understand these kind of systems, experiments carried out in drops are an excellent model system.

1.4 Drop confinement

Numerical simulations [2] and experiments [29] show that active nematic particles in spherical drops organize vortices (Fig.1.4a Top) and depending on the parameters a ring around the equator can be formed (Fig.1.4a Bottom). Numerical simulations in 2D show that de-

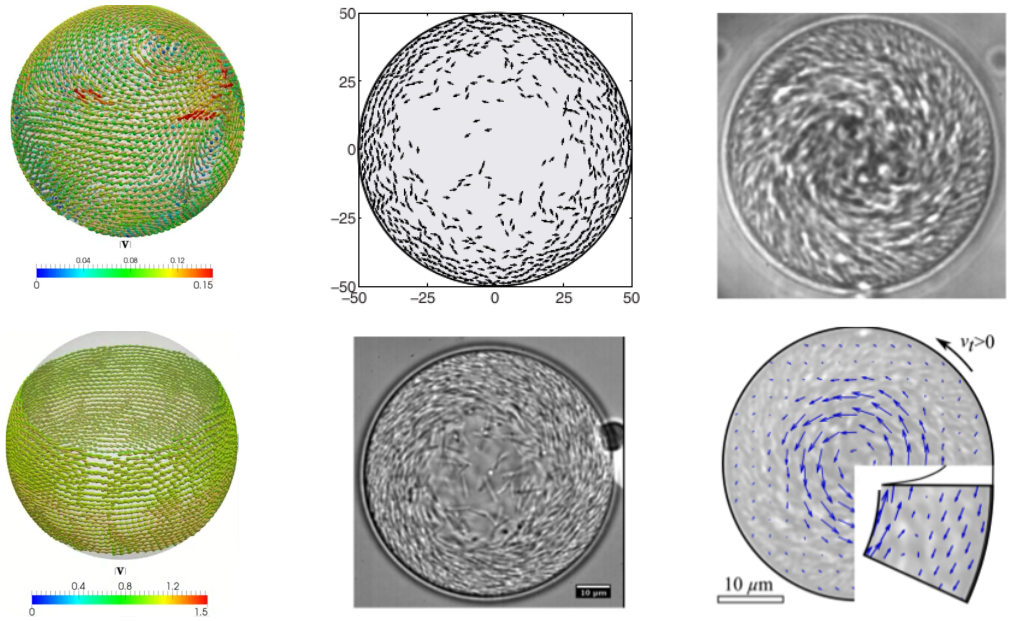

(a) (b) (c)

Figure 1.4: (a) Top: Numerical simulation of nematic particles confined on the surface of a sphere. Two vortices can be noticed on the right of the sphere. Similar vortices have been observed on high concentrated *E. coli* confined in a drop. Bottom: In the same simulation, there is a stable state where a ring around the equator of the sphere is predicted. This kind of ring has been observed in active nematic microtubules confined in a droplet (Modified from the supplementary material of Sknepnek & Henkes [2]). (b) Comparison between numerical simulation (Top) and experiments performed with *B. subtilis* (Bottom). A strong confinement can be noticed on the border where a band with stable circulation appears. Top image modified from Cheng Hou Tsang & Kanso [20] (c) Top: Increasing the amount of bacteria in the suspension, the formation of a stable vortex in the center of the circular geometry can be observed. Bottom: The velocity field of the bacterial suspension is shown. It is clear the difference between the rotation of the central vortex (counter-clockwise) versus the circulating band on their border (clockwise). (b) Bottom and (c) from Wioland *et al.* [28].

pending on the flagellar activity, microswimmers confined in a circular geometry can exhibit collective motion, circulating near the border (Fig.1.4bTop)[20], similar to the behavior experimentally observed in a quasi 2D system, where a bacterial suspension of *Bacillus subtilis* is confined inside a *pancake-like* droplet (Fig.1.4b Bottom). In this experiment [28], there is a stable spiral vortex in the center of the circular geometry (Fig. 1.4c). In the case of a bacterial suspension of *E. coli* confined inside a spherical droplet, strong accumulation on the inner surface is observed, and at higher bacterial concentration collective motion appears, presenting several vortices [19].

1.4.1 Work extraction from the active suspension

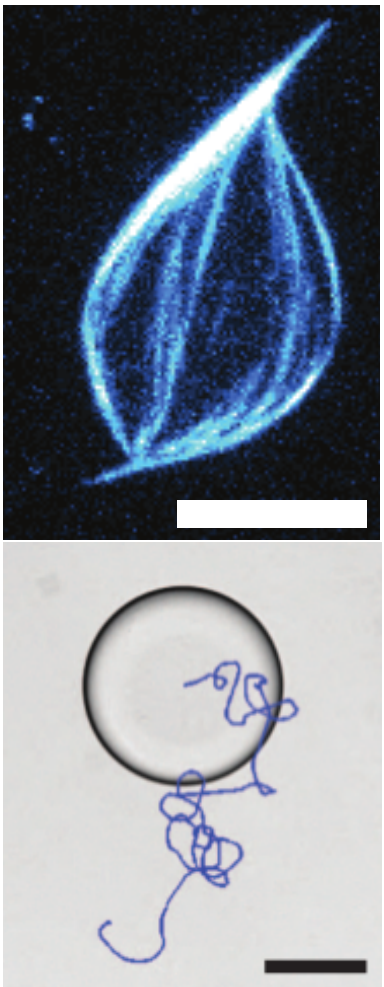

Figure 1.5: Top: Deformation of an active microtubule vesicle. Scale bar 8µm.(From Keber *et al.*[29]) Bottom: Trajectory performed by an active microtubular droplet during 33min. Scale bar is 80µm (From Sanchez *et al.* [30])

Experiments encapsulating microtubules and kinesin motors in droplets show that they deform and move the confining drop (Fig.1.5), what is an interesting example of how the system extracts work from the active suspension to generate movement, similar to microorganisms, that extract work from molecular motors to drive internal processes, such as the rotation of flagella.

Following this example, one could extract work from an encapsulated bacterial suspension as well. As we discussed, individual bacteria can be characterized by a thrust force of magnitude $f \sim \eta \ell v_0$, where v_0 and ℓ are the characteristic speed and size of the bacterium, and η the viscosity of the ambient fluid. Hence, in a suspension with a volumetric concentration n of bacteria, there exists a potential to extract a mechanical power $P \sim nfv_0$ per unit volume. Using typical values for *Escherichia coli* (*E. coli*), $f \approx 0.5\,\mathrm{pN}$ [11] and $v_0 \approx 20\,\mu\mathrm{m/s}$ in aqueous media, and for a relatively dense suspension of $n \approx 10^{10}$ bact/mL ($\sim 1\%$ in volume fraction), one obtains $P \sim 0.1\,\mu\mathrm{W/mL}$. Also, bacteria confined inside the drops are unable to escape or deform the drop surface, as can be easily understood from an energy balance. The energy required to create a bump of size comparable to the bacterial body in the drop surface is $\sim \gamma/\ell^2$, with γ the interfacial tension, while the energy that a bacterium spends by swimming the same distance is $f\ell \sim \eta \ell^2 v_0$. The ratio between these two energies is of the order of the capillary number, $Ca = \eta v_0/\gamma \sim 10^{-5}$, considering a typical water/oil interfacial tension in the presence of surfactants, $\gamma \sim 1\,\mathrm{mN/m}$. As a result, bacteria swimming near a typical water/oil interface feel a rigid boundary and thus behave similarly than when they swim near a solid wall [31] or a free surface [32]; they interact with their hydrodynamic image and accumulate at the interface. This accumulation near the drop interface [33, 19] can enhance the interaction of the bacterial flows in the drop and the fluid surrounding the drop.

From the previous discussion, we can realize that encapsulating bacterial suspensions in drops is an interesting system to test extraction of useful work and active matter properties. Thus, the general objective of this thesis[1] is to study and describe the dynamics of bacteria confined inside a drop. Are we able to form a "motor made of motors" [30] from the bacterial suspension? can we extract energy from this bacterial motor? How are the collective motions inside the drops? can we control this motion from an external field? The methodology to answer these questions, is preparing a water-in-oil emulsion, where the water phase is the bacterial suspension, and then observing the drops in the microscope. We performed three experiments where bacteria are confined within the drop, which we describe in the following.

In the first experiment, we study a dense suspension of motile Escherichia coli inside a spherical droplet in a water-in-oil emulsion [34]. This work was carried out at the Microfluidics lab at the DFI/FCFM of the University of Chile. We show that bacterial flows are able to transfer movement to the drop, which performs a persistent random walk. Organized collective motion of bacteria [28] and their accumulation at the drop interface [19] are key ingredients in our work. At high concentration, bacteria organize in turbulent-like, chaotic collective motions known as active turbulence [35, 10]. Microswimmers such as *E. coli* swim by exerting a force dipole on the ambient fluid, and are thus force and torque free [36]. Moreover, the chaotic bacterial flow inside the drops is indeed isotropic and should average to zero, both spatially and temporally. Therefore, the transfer of motion to the drops is not intuitive. In fact, drops sit over a substrate separated to it by a thin lubrication film, and this spatial symmetry breaking is necessary for the movement of the drops. We show that the drop movement and its direction is determined by the bacteria that move near the substrate, causing the drop to roll over the substrate. The turbulent-like motion of the bacterial bath constantly changes the direction and speed of the bacteria that swim near the bottom of the drop. This explains both the persistent movement of the droplets at short times and their random motion at long times.

In the second experiment, we study aqueous spherical droplets suspended in oil and containing a suspension of magnetotactic bacteria [37]. This work was carried out at the PMMH-ESPCI, France, along with Benoit Vincenti under the direction of Carine Douarche and Eric Clement, and in Chile. In this work, we show how MTB self-assemble into a rotary motor under the application of a uniform and constant magnetic field, providing a mechanical torque to the fluid outside the droplets. In the self-assembly process, the magnetic field induces an accumulation of the swimming bacteria in diametrically opposed areas at the surface of the droplet. At high bacterial concentration, the flows resulting from the swimming activity of the bacteria and originating from these areas, interact to create a collective solid-like vortex flow in the central droplet core. Through Particle Image Velocimetry (PIV) analysis and particle tracking, we quantify the flows inside and outside the droplet and measure the net torque produced by this micromotor as a function of the magnetic field and the droplet radius. Also, we provide an explanation on how an external torque can be generated despite the fact that the swimmers self-propel at almost zero Reynolds number.

[1]Financed by CONICYT-PFCHA Doctorado Nacional 2015 21150648

Finally, we study a bacterial suspension of *E.coli* encapsulated in a double emulsion, where an oil droplet gets trapped inside a water in oil emulsion. This work was carried out between the Gulliver lab and the PMMH, both at the ESPCI in France. The experiments were performed along with Martyna Goral under the direction of Teresa Lopez-Leon, Anke Lidner and Eric Clement. In this work we present a protocol for making double emulsions, and preliminary results about the persistent random walk performed by the inner oil droplet, and finally, we measure an *active temperature* of the bacterial bath. New experiments are being performed in Chile by Cristian Villalobos under the direction of Maria Luisa Cordero and Rodrigo Soto, that will complete this work in the future.

Chapter 2

Bacterially Propelled Droplets

2.1 Methods and Protocols

2.1.1 Bacterial culture

We use a run and tumble strain of *E. coli* (W3110) which is also genetically modified to express the green fluorescence protein (GFPmut2)[38]. Bacteria are collected from a $-20\,^{\circ}\mathrm{C}$ stock (Appendix A.3) and grown overnight in rich Luria-Bertani medium (LB) (Appendix A.1) at $28\,^{\circ}\mathrm{C}$ with an agitation of 180 rpm. From this sample, 1 mL of overnight is diluted in 9 mL of LB. The suspension is again incubated at $28\,^{\circ}\mathrm{C}$ with agitation of 180 rpm and harvested in the exponential phase of the growth curve when it reaches an optical density at 600 nm (OD) of 0.7 ± 0.1. The suspension is centrifuged at 3000 rpm for 15 minutes, and the pellet is then washed and diluted in a phosphate motility buffer, MMA (Appendix A.7) [39]. The motility buffer MMA is a controlled environment where bacteria can swim but do not divide [5]. The concentration of the final bacterial suspension, n, ranges from 5.14×10^8 to 2.25×10^{10} bact/mL, depending on the amount of MMA added after centrifugation. In the case of lowest concentration reached, 500 µL of MMA was added and for the maximum concentration 8 µL of MMA.

A volume of 10 µL of the bacterial suspension is added to 1 mL of Hexadecane containing Span80 (2% in weight) as a surfactant. The mixture is manually agitated, resulting in an emulsion of aqueous droplets containing the bacterial suspension in oil (Fig. 2.1). The radii of the droplets, R, are widely dispersed, between approximately 10 µm and 200 µm.

2.1.2 Experimental Setup

The observation setup is a square chamber of inner side $L = 1$ cm and height $h = 400$ µm. The chamber walls are fabricated in SU-8 photoresist (Gersteltec GM 1075) by optical lithography (Heidelberg Instruments MLA 100) on a 50.8 mm diameter and 500 µm thick circular glass

wafer (University Wafer Borofloat 33). After chamber fabrication, the bottom of the chamber is hydrophobically treated using a siliconizing reagent (Sigmacote, Sigma-Aldrich).The emulsion is poured inside the chamber (Fig. 2.1) and then the chamber is sealed by a coverslip to minimize evaporation and flows in sample. As the aqueous bacterial suspension is denser than the ambient hexadecane, drops sediment to the bottom of the chamber, but remain separated from the substrate by a thin hexadecane lubrication film, whose thickness we estimate at $\varepsilon \approx 20\,\mathrm{nm}$ [40]. The chamber is placed on an inverted microscope (Nikon TS100F) and filmed by a camera (Andor Zyla 2048×2048 pix^2) at 50 fps. Low magnification (10X/0.25 NA objective) in bright field is used to record the movement of several drops simultaneously. High magnification (40X/0.60 NA objective) in fluorescence is used to observe the bacterial flows inside the droplet.

Image analysis is performed with homemade MATLAB scripts to track the droplets and to analyze the drops trajectories. Particle image velocimetry (PIV) is performed with the Matlab Toolbox PIVlab [41], in order to obtain the velocity field inside the drops.

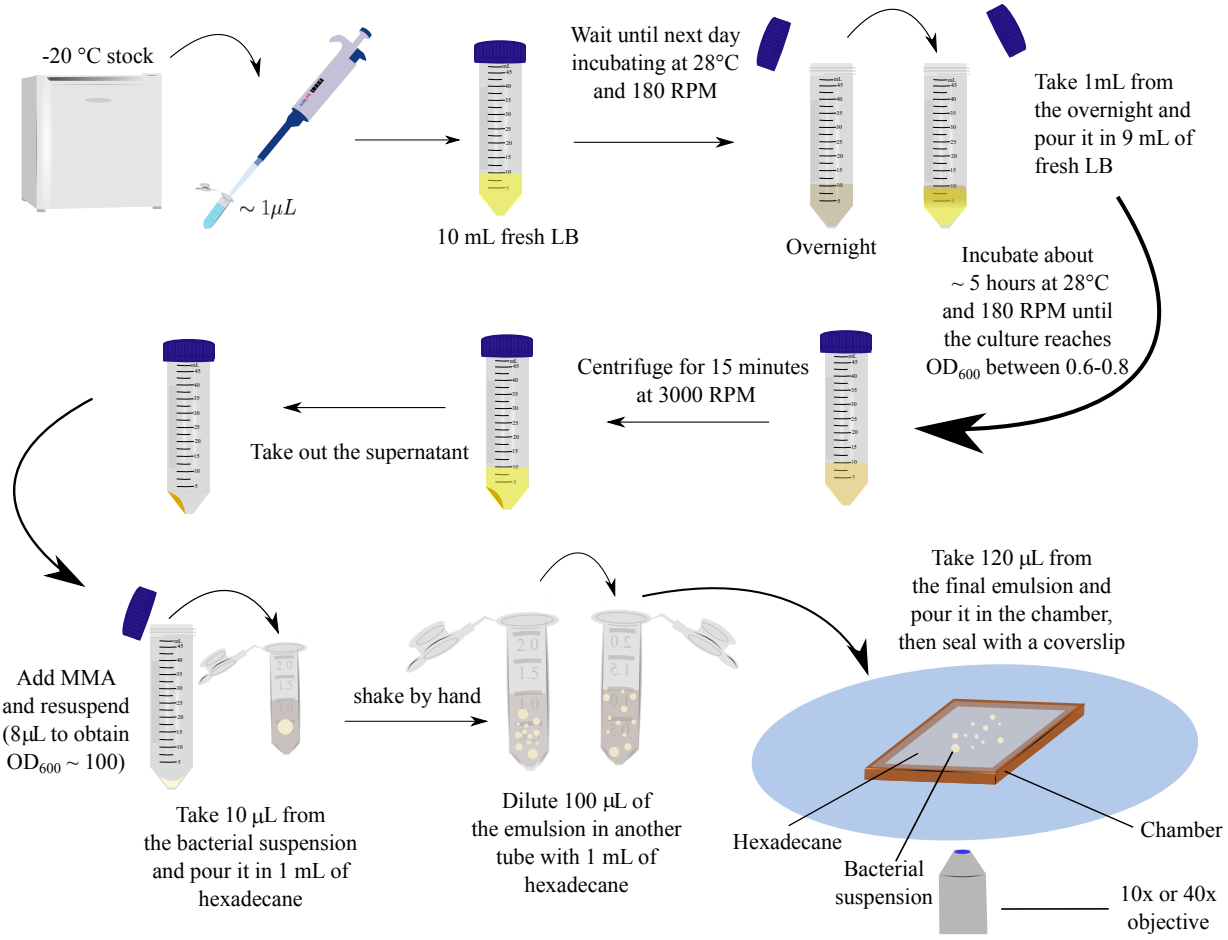

Figure 2.1: Steps to prepare the bacterial emulsion

2.1.3 Image analysis

Tracking Analysis

We developed our own tracking script for droplets, which takes into account the size distribution. The tracking script works as follows. First, we perform a morphological opening, which consists of an erosion followed by a dilation in the grayscale image, using a 5 pixel radius disk, as a structuring element for the morphological operation. This improves the contrast between droplets and the background. Then, we profit the matlab function *imfindcircles*, which is programmed to find several circles of different radii using the Hough transform. It goes over the whole image sequence, finding all centers and radii (Fig.2.2a). In order to assign *names* to trajectories, the image containing all positions of all drops detected during the whole image sequence is binarized. Then, a morphological dilation is performed, merging the points of a complete track into a single structure (Fig.2.2b). It is important to notice that there is no crossing between two drops trajectories. Each structure corresponding a drop trajectory is labeled, and then the points of the trajectory are ordered in time. After the tracking process, defective tracks are filtered (e.g. tracks shorter than 1 minute), the tracks are smoothed to reduce noise, and values are converted from pixels to microns. First, the mean square displacement is computed and then the droplet's instantaneous velocity **V**.

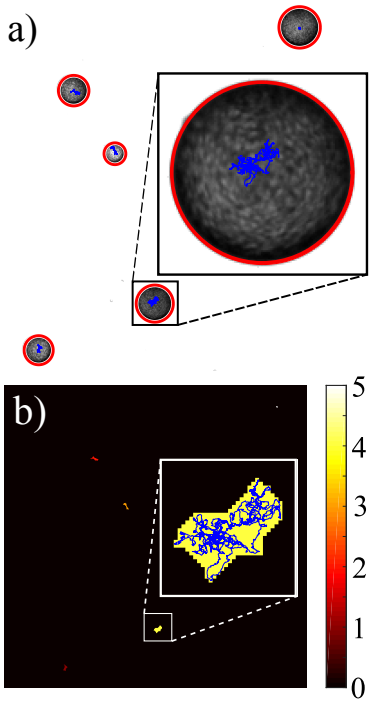

Figure 2.2: a) Representative image of bacterial drops observed with a 10X objective. The red circles are the detected drops by the *imfindcircles* function. Blue lines are the centers detected over the image sequence. b) The centers are grouped into regions, (yellow in zoom) to label and assign droplets to tracks (blue lines). Color scale corresponds to labels of tracks.

PIV Analysis

In the case of drops, filmed with the 40X objective, the tracking method is similar, but the code looks for just one single drop and then it performs the same algorithm to the tracks to obtain velocity, MSD, etc. Then, the images are prepared for the PIV analysis. In order to obtain an internal velocity field without the influence of the droplet's movement, the image is treated, letting the droplet always in the center. This is achieved by cropping all images with the same size, measured from the center of the droplet. The centering algorithm is as follows. In the first image, the droplet is detected and a binary circle with the same features is defined, and a crop on the image is done. Then, a 2D cross correlation between every image with the initial binary image is performed, finding the coordinates of the maximum value of the correlation, which is employed to center the droplet to finally crop it with the same size of the binary image (Fig.2.3). The process previously described, allows us to have the image sequence of a droplet as if it were fixed.

Before doing PIV on the image sequence, we select the brightest part of the image, and for calculation purposes we chose an observation region of radius $R_{obs} = \sqrt{7}R/4$ that corresponds to a height $h_{obs} = \frac{1}{4}R$ measured from the bottom. A binary image of a circle of radius R_{obs} is then created in *imageJ*, to be applied as a mask. Before applying the mask, the image contrast is enhanced dividing each image by its own Gaussian filter, and on the resulting image, a *Wiener2* filter is applied, to get rid of spurious noise. Finally, the image is multiplied by the mask, in order to have just the region where PIV will be done, and the rest of the image is zero (Fig.2.4). Now, PIV is performed using PIVlab, with a window size of 10 µm, and a step of 5 µm. We allow a second pass as well, with a window size of 5 µm.

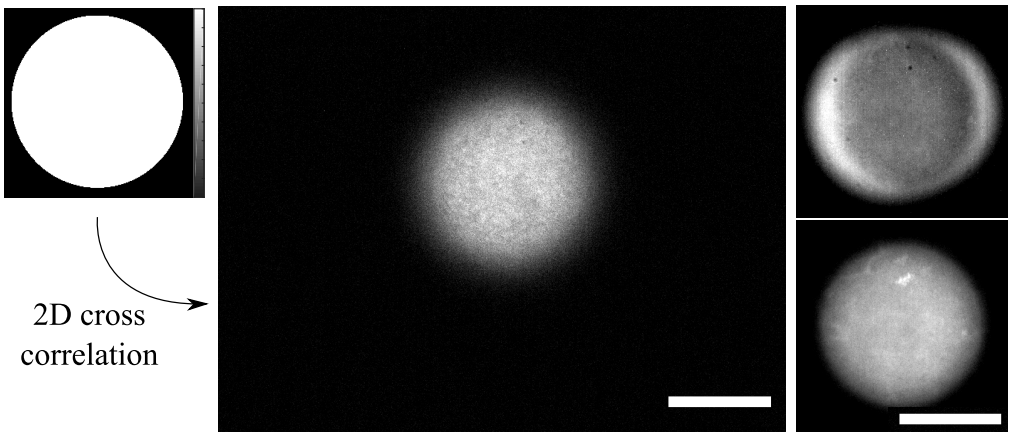

Figure 2.3: Schematics of the centering process of drops before PIV. The mask of the drop (left) is applied over the raw image (center image). Color scale corresponds to pixel intensity of the binary image, where black is zero and white is 1. The results are presented with the average of the whole image sequence (right). Without applying the mask (Top right) and applying the mask (Bottom right). Scale bar 30 µm

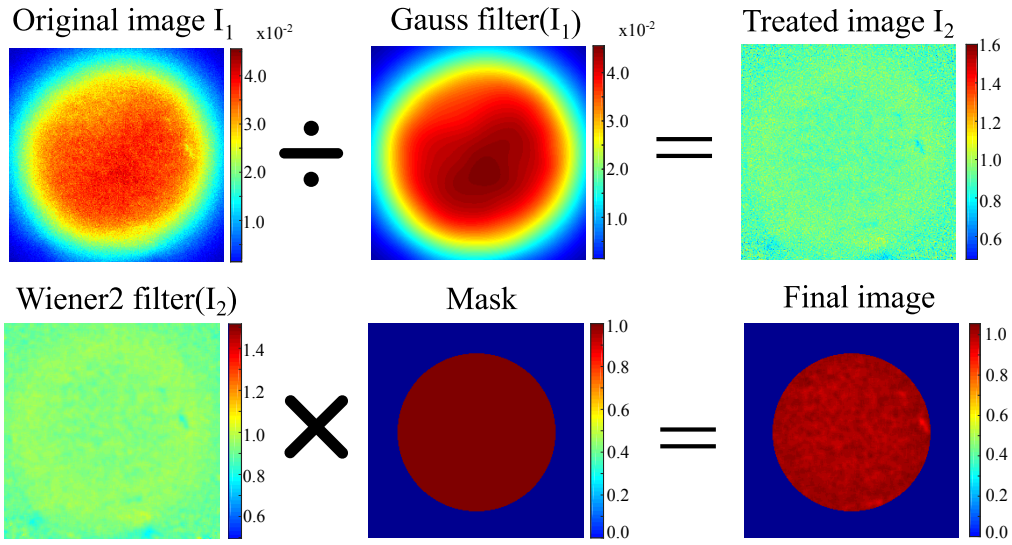

Figure 2.4: Image treatment to enhance the region of PIV analysis. Color scale is intensity of image.

2.2 Results

Immediately after the emulsion is poured inside the chamber, observation at the microscope reveals a continuous and erratic movement of the droplets. Closer inspection of the drops reveals the existence of collective motion of the bacteria inside the drops, generating a complex inner flow. This flow organizes in vortices that appear, move and disappear continuously, indicative of active turbulence [35]. The movement, both of the drops as a whole and of the bacterial suspension inside the drops, can last several minutes up to several hours. Typically, droplets of radius smaller that 20 µm stop moving after a few minutes, and larger drops move for larger times. We hypothesize that consumption of oxygen or nutrients, or the accumulation of bacterially-generated waste, which happens faster in smaller drops, can cause the bacteria to eventually stop swimming and drops no longer displacing. Figure 2.5a shows the trajectory of a drop of radius $R = 27\,\mu\text{m}$ and bacterial concentration $n = 1.68 \times 10^{10}$ bact/mL for approximately 4 minutes. Note that the maximum displacement of the drop can be larger than R. From the tracked trajectories, it is possible to determine the instantaneous velocity averaging over 5 temporal steps. Figures 2.5b-c display the temporal evolution of the speed as well as the measured speed distribution function for the same droplet. The speed is highly fluctuating with a distribution that resembles a Gaussian. Its temporal correlation, which is quantified below, is of the order of a fraction of a second, which is larger than the acquisition time interval $1/50\,\text{s}$, allowing us to extract the instantaneous velocities.

2.2.1 Persistent random walk

A total of 991 drops, with radii ranging from $R \approx 20\,\mu\text{m}$ to $R \approx 120\,\mu\text{m}$ are tracked for 1 minute. Smaller drops are not tracked because they lose their movement too rapidly, and larger drops are discarded to avoid interactions with the upper coverslip. From each droplet trajectory, the mean square displacement (MSD), $\langle \Delta \mathbf{x}^2 \rangle$, is calculated (Fig. 2.5d). MSD curves indicate that drops perform a persistent random walk, with a ballistic motion for small times and a diffusive motion at larger times. The shape of the MSD is very well fitted with [42]

$$\langle \Delta \mathbf{x}^2 \rangle = 4D\tau \left(\frac{t}{\tau} - 1 + \mathrm{e}^{-t/\tau} \right), \tag{2.1}$$

where D is the long-time diffusion coefficient of the droplet and τ the persistence time of the ballistic motion. From eq. (2.1), D and τ for each droplet are extracted. The instantaneous speeds, V, are averaged over the whole trajectory duration to obtain a mean drop speed, $\langle V \rangle$, for each droplet.

The observations present a wide variability; droplets with the same radius and bacterial concentration can present very different values of $\langle V \rangle$, τ, and D. Despite this variability of the data, individual values of D, $\langle \mathbf{V}^2 \rangle$ and τ for each droplet collapse in the line $D = \alpha\tau \langle \mathbf{V}^2 \rangle$ (Fig. 2.5e). For a persistent random walk with a velocity autocorrelation function $\langle \mathbf{V}(t) \cdot \mathbf{V}(0) \rangle = \langle \mathbf{V}^2 \rangle \exp(-t/\tau)$, it is obtained that $\alpha = 1/2$ (see Ref. [42]). The best fit gives $\alpha = 0.57 \pm 0.01$. The difference with the persistent random walk prediction

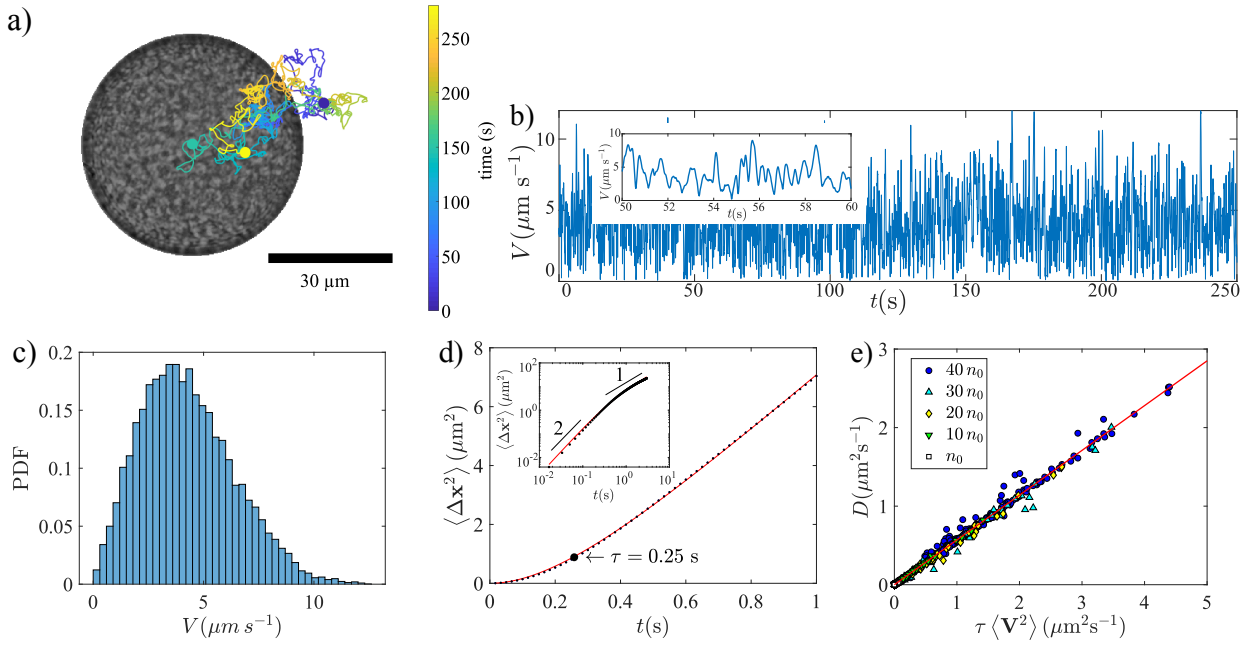

Figure 2.5: a) Trajectory of a droplet ($R = 27\,\mu$m and $n = 1.68 \times 10^{10}$ bact/mL) observed in bright field for about 4 minutes. The trajectory is represented by the colored line, with the color scale representing the time from the start (blue dot) to the end (yellow dot). The image of the droplet corresponds to its position 150 s after the initial time (green dot). The high bacterial concentration prevents to distinguish individual *E. coli* inside the drop. b) Instantaneous speed of the droplet in a). The inset shows a small temporal windows to appreciate the temporal scale of variations. c) Velocity distribution function for the same droplet. d) Representative example of MSD (same droplet as in a)). Little black dots are experimental data and the red line is the fit using equation (2.1). Persistence time is indicated with the arrow. The inset shows the same data in log-log scale. The two lines are power laws with exponents 2 and 1. The R-squared for the fitting is 0.99. e) Measured diffusion coefficient D as a function of $\tau \langle \mathbf{V}^2 \rangle$ for all measured drops (991 drops). The data for different bacterial concentration collapse in a straight line with slope $\alpha = 0.57$ (red line). The R-squared for the fitting is 0.99. The reference concentration is $n_0 = 5.14 \times 10^8$ bact/mL.

suggests that the velocity autocorrelation function is not a single exponential, but the experimental precision does not allow to discriminate among different models.

2.2.2 Dependence on bacterial concentration

The movement of droplets was studied as a function of the bacterial concentration n in the bacterial suspension. Droplets with radii from 20 µm to 30 µm were selected, obtaining between 100 and 170 drops for each bacterial concentration. The average diffusion coefficient, persistence time and average speed were calculated at each concentration, as shown in Figs. 2.6a-c. Although dispersion remains high, an increasing tendency of D with n can be

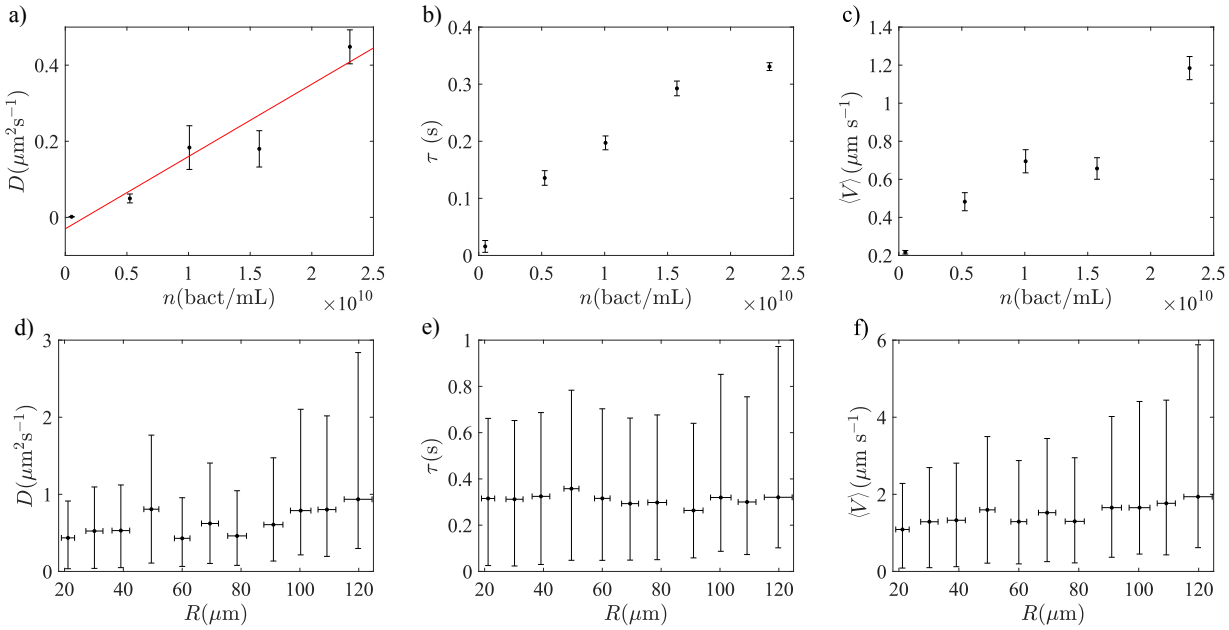

Figure 2.6: a) Diffusion coefficient, b) persistence time, and c) mean speed as a function of bacterial concentration, averaged for droplets with radii in the range 20 µm to 30 µm (100 to 170 drops for each bacterial concentration). Symbols represent experimental data and the red line in a) corresponds to a linear fit with R-squared 0.91. d) Diffusion coefficient, e) persistence time, and f) mean speed as a function of droplet radius for fixed bacterial concentration $n = (2.25 \pm 0.14) \times 10^{10}$ bact/mL. The drops are grouped within windows of increasing radius in 10 µm increments. For a-c, the error bars indicate the standard error around the mean value, while in d-e, the horizontal error bars represent the standard deviation on drop radius and the vertical error bar is the confidence interval at 63%.

observed. Data was fitted to a linear curve $D = D_0 + D_1 n$, with $D_0 = (-0.03 \pm 0.15)$ µm^2/s and $D_1 = (19 \pm 11)$ µm^5/s/bact. The persistence times and the average speed also increase with the bacterial concentration.

2.2.3 Dependence on the drop radius

To analyze the dependence with the droplet radius, we consider the case of maximal bacterial concentration, $n = (2.25 \pm 0.14) \times 10^{10}$ bact/mL, and the drops are grouped within windows of increasing radius in 10 µm increments. The results for D, τ, and $\langle V \rangle$ as a function of R are presented in Figs. 2.6d-f. For each radius window, a large variability exists for the diffusion coefficient, the persistence time and the average drop speed. The average diffusion coefficient and persistence time remain approximately constant at $D \sim 0.5$ µm^2/s and $\tau \sim 0.3$ s. The average speed increases slightly with the drop radius and its average value is $\langle V \rangle \sim 1.5$ µm/s.

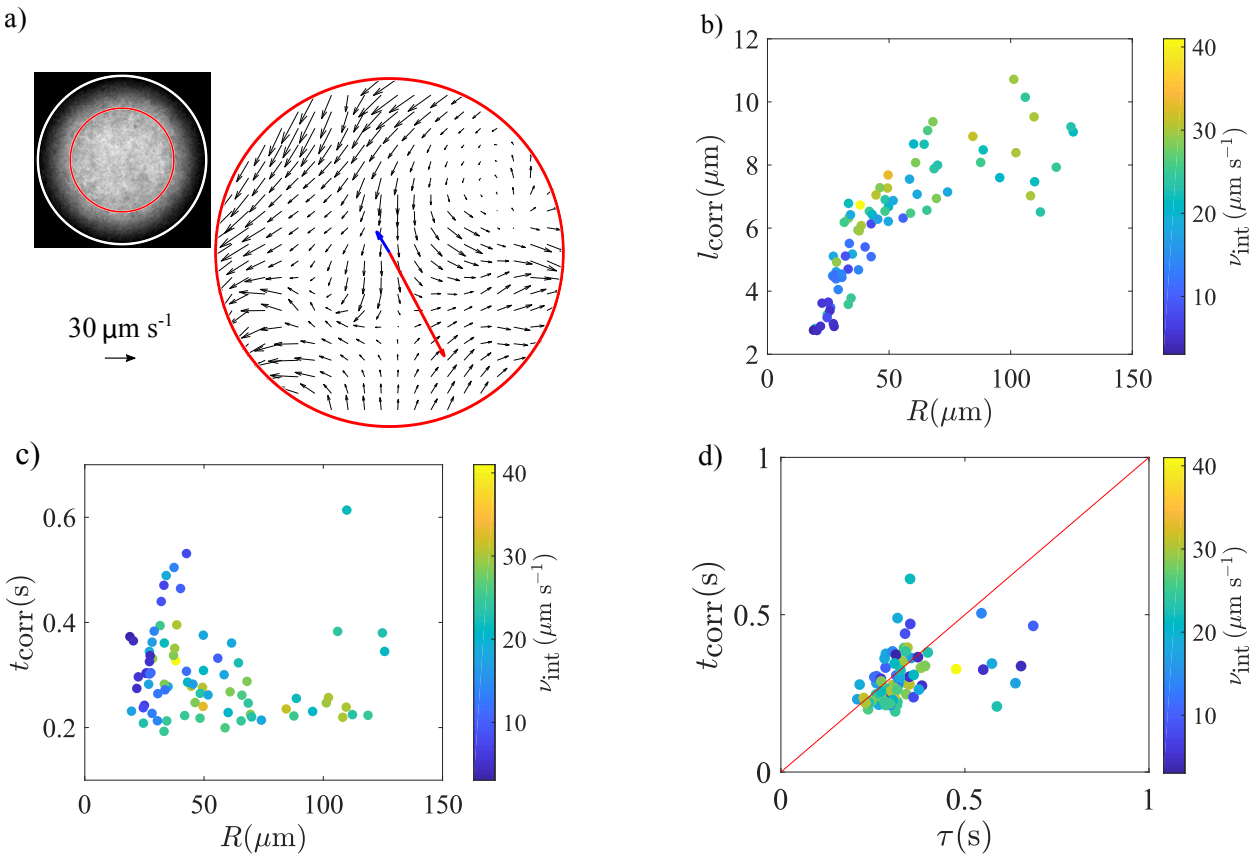

Figure 2.7: a) Velocity field in the bottom part of a drop, obtained by PIV (black arrows). The red arrow is the weighted average internal velocity $\mathbf{v}_b$, while the blue arrow is the instantaneous velocity of the droplet $\mathbf{V}$. For clarity, the red and and blue arrows are enlarged by a factor 10 with respect to the scale. The inset shows a fluorescence image of the bottom part of a drop. The outer white circle marks the boundary of the droplet, of radius $R = 28\,\mu\text{m}$. The PIV analysis was performed within the inner red circle of radius $R_{\text{obs}} = 18\,\mu\text{m}$. b) Correlation length l_{corr} and c) correlation time t_{corr} for the velocity field inside the droplets as a function of drop radius R and mean speed of the internal flow, v_{int} (color scale). d) Correlation time of the internal flow, t_{corr}, compared with the persistence time of the drop motion, τ. The red straight line has slope one and is a guide to the eye.

2.2.4 Internal flows

Internal flows in the bottom of the drops were recorded in fluorescence near the contact surface with the substrate. Fluctuating vortical flows driven by the bacterial activity are observed. Velocity fields $\mathbf{v}(x, y, t)$ are obtained with PIV in a small region of the bottom of the drops, corresponding to the brightest portion of the image. For calculation purposes, we chose an observation region of radius $R_{\text{obs}} = \sqrt{7}R/4$ that corresponds to a height $h_{\text{obs}} = R/4$ measured from the bottom (Fig. 2.7a).

Several drops are measured and, from each velocity field, the mean speed of the internal flow $v_{\text{int}} \equiv \langle|\mathbf{v}(x, y, t)|\rangle$ is computed, where the average is over time and space. Also, the average over time of the correlation length l_{corr} for the velocity field is calculated as described in

Ref. [43]. The dependence of $l_{\rm corr}$ on drop radius R and mean internal speed $v_{\rm int}$ is presented in Fig. 2.7b. For drop radius between 20 µm and 50 µm, $l_{\rm corr}$ increases rapidly from ≈ 3 µm to ≈ 7 µm, with relatively little dispersion. For larger drop radius, $l_{\rm corr}$ seems to plateau at a value of ≈ 8 µm, but with larger dispersion. The dependence of $l_{\rm corr}$ on $v_{\rm int}$ (color scale of Fig. 2.7b) presents a larger dispersion, but in general $l_{\rm corr}$ increases with $v_{\rm int}$.

Finally, the correlation time of the velocity field, $t_{\rm corr}$, was obtained as follows. For each position in the observation region, the temporal self-correlation function of the velocity is obtained. From it, we compute the first moment, and the average of these give $t_{\rm corr}$. Figure 2.7c shows that the correlation time is almost insensitive to the droplet radius, with a mean value of $t_{\rm corr} = (0.30 \pm 0.08)$s. Also, the correlation time, $t_{\rm corr}$, is compared with the persistence time, τ (Fig. 2.7d). Their values are not equal but they have the same order of magnitude.

2.3 Discussion

2.3.1 Bacterial activity enhances droplet diffusion

Thermal diffusion of a sphere of radius R in a medium of viscosity η at temperature T is given by $D_{\rm th} = k_{\rm B}T/(6\pi\eta R)$. In the case of a liquid drop of viscosity η', a factor $C(\eta'/\eta)$ must be included,

$$C(\eta'/\eta) = 6\pi \left(\frac{2/3 + \eta'/\eta}{1 + \eta'/\eta} \right). \tag{2.2}$$

This factor accounts for the slip condition at the drop surface, yielding $D_{\rm th} = k_{\rm B}T/[C(\eta'/\eta)\eta R]$ [44]. Using $\eta' = 1\,$mPa s for water and $\eta = 3.47\,$mPa s for hexadecane, gives $C = 13.9$. With $T = 20\,^{\circ}$C and $R = 20\,$µm (the smallest radius considered here), we obtain $D_{\rm th} \approx 0.4 \times 10^{-2}\,\mu$m^2/s. This value is two orders of magnitude smaller than the average diffusion coefficient $D \approx 0.3\,\mu$m^2/s that we measure for drops at the higher bacterial concentration used here. For a droplet of mass M, its stopping time in hexadecane is $\tau_{\rm stop} = M/[C(\eta'/\eta)\eta R]$. The same parameters used to estimate $D_{\rm th}$ give $\tau_{\rm stop} = 3.3 \times 10^{-5}\,$s, which is much smaller than the persistence time τ of the ballistic motion of the drops.

Our results do not evidence any significant dependence of the diffusion coefficient with the drop radius (Fig. 2.6d), as opposed to the $1/R$ scaling of $D_{\rm th}$. This is also true for the mean persistence time τ (Fig. 2.6e). The mean droplet speed $\langle V \rangle$ (Fig. 2.6f), exhibits a slight increase with the drop radius that could be due to the loss of bacterial activity, which occurs faster for smaller droplets.

Finally, diffusivity of the droplets increases linearly with the concentration of the bacterial suspension (Fig. 2.6a). The intercept found with the linear fit is consistent with the thermal diffusivity $D_{\rm th}$ expected for drops in the size range studied here.

These observations indicate that bacterial activity is the motor of the movement that we observe in the drops. In the following we present a model to explain the drop movement based on the internal flows driven by the bacteria.

2.3.2 Driving mechanism

In dense suspensions, swimming bacteria usually organize in collective motions. Inside the spherical drops that we study, these collective motions translate in vortices that appear, move and disappear continuously, with a characteristic size $l_{\rm corr}$ and life time $t_{\rm corr}$. The value of $l_{\rm corr}$ shows an increasing tendency with the drop radius, probably related to confining effects (Fig. 2.7b). Comparison of the characteristic duration of these collective motions with the persistence time of the ballistic motion of the droplet (Fig. 2.7d) reveals that both are restricted to the same range, around 0.3 s.

Experimental results indicate that the bacterial motion inside the drops is responsible for the movement of the drops. The bacterial currents are highly fluctuating, with correlation lengths smaller than the droplet radii. Hence, if the droplet were suspended in an infinite fluid medium, the drag forces on different regions of the droplet surface would almost cancel out, resulting in small instantaneous values. We hypothesize that the presence of the bottom glass substrate, on the contrary, enhances the drag effect of these fluctuating currents. In effect, only a small region of the droplet is in contact with the substrate, where it is more probable to observe coherent motion. As the friction close to the solid surface becomes larger, the cancelation of the drag forces described above does not take place. The mechanism that we propose is a "rolling with slipping". When the bacterial motion inside the drops produces a patch of directed flow in the lowest part of the drop, the thin lubrication film existing between the glass substrate and the drop is sheared in the direction of the flow. This shear, in turn, creates a net force on the drop that causes its movement in the opposite direction of the inner flow, as schematically shown in Fig. 2.8a. By lubrication theory, we can approximate the motion of the bottom part of the droplet as having an angular velocity $\Omega = v_{\rm b}/R$, where $v_{\rm b}$ is the speed of the inner flow at the bottom of the drop. Note that we are not assuming that the droplet rotates as a whole because only the bottom region of the droplet is relevant for the lubrication theory calculation Considering that the droplet moves at a velocity $\mathbf{V}$, the total hydrodynamic force on the droplet is $\mathbf{F}^{\rm hydro} = \mathcal{R}^{FU}\mathbf{V} + \mathcal{R}^{F\Omega}\mathbf{\Omega}$, where $\mathcal{R}^{FU}$ and $\mathcal{R}^{F\Omega}$ are resistance tensors, which depend on the lubrication layer thickness ε [21]. At vanishing Reynolds number, the hydrodynamic force cancels, resulting in

$$\mathbf{V} = -\frac{\mathcal{R}^{F\Omega}_{/\!/}}{R\mathcal{R}^{FU}_{xy}}\mathbf{v}_{\rm b} = -\left(\frac{2\ln(\varepsilon/R)/15 + 0.2526}{8\ln(\varepsilon/R)/15 - 0.9588}\right)\mathbf{v}_{\rm b}, \tag{2.3}$$

where we used the expressions for the resistance tensors in Ref. [21]. In eq. (2.3), $\mathbf{v}_{\rm b}$ is the relevant velocity at the bottom of the drop, caused by the bacterial motion and the minus sign indicates that the drop velocity $\mathbf{V}$ is antiparallel to $\mathbf{v}_{\rm b}$.

To test this hypothesis, we define a weighted average internal velocity $\mathbf{v}_b$, with a weight function $w(x, y)$,

$$w(x, y) = \frac{1}{h(x, y)^2 + \varepsilon^2}, \tag{2.4}$$

where (x, y) represent the horizontal coordinates of a point in the PIV velocity field, $h(x, y)$ is the height from the lowest point of the droplet to the interface at position (x, y) (see Fig. 2.8a). The square in h is used to give more weight to the points near the glass surface and roughly models the decay of the flow produced by force dipoles. ε is a regularizer to

avoid divergences and is estimated to be of the order of the lubrication film thickness. We take $\varepsilon = 20\,\mathrm{nm}$. Then,

$$\mathbf{v}_\mathrm{b}(t) = \frac{\sum_{x,y} \mathbf{v}(x,y,t) w(x,y)}{\sum_{x,y} w(x,y)}. \tag{2.5}$$

This weighted average velocity is compared with the velocity of the droplet $\mathbf{V}$ obtained by the drop tracking. Figure 2.8b shows our experimental results of $\langle V \rangle / v_\mathrm{b}$ as a function of R, together with the slippery rolling model, eq. (2.3). Despite the variability in the experimental data, the agreement between the experiment and the model is very good, except for the smallest droplets.

In general, $\mathbf{v}_\mathrm{b}$ and $\mathbf{V}$ go in opposite direction, as shown by the red and blue arrows in Fig. 2.7a, respectively. To quantify this antiparallel behavior, the angle θ between $\mathbf{v}_\mathrm{b}$ and $\mathbf{V}$ is determined in the range $[0, 2\pi]$ along the whole trajectory for all droplets. The probability density function (PDF) of θ is presented in Fig. 2.8c. A peak near $\theta = \pi$ is clearly evident. The location of the peak and the width of the distribution is determined by fitting a von Mises distribution

$$P(\theta) = \frac{1}{2\pi I_0(k)} \mathrm{e}^{k\cos(\theta - \theta_0)}, \tag{2.6}$$

where I_0 is the modified Bessel function of the first kind and $\theta_0 = \pi + \delta$ is the position of the center of the distribution, with δ the deviation from the perfect antiparallel alignment between $\mathbf{v}_\mathrm{b}$ and $\mathbf{V}$. Finally, k is a measure of the width of the distribution. For $k = 0$ the distribution is uniform and for $k \neq 0$ it is more concentrated in a certain angle. Fitting of the PDF with the von Mises distribution yields $k = 0.80$ and $\delta = -0.0015$ (Fig. 2.8c, red line). Since $\delta \ll \sqrt{k}$ and $P(\pi)/P(0) = \exp(2k) \gg 1$, the vectors are, on average, effectively antiparallel.

Another way to prove and test our hypothesis, is to inverse the weight function, giving more importance to the outer part of the velocity field,

$$w(x,y) = 1 - \frac{1}{h(x,y)^2 + \varepsilon^2}. \tag{2.7}$$

We compute $\mathbf{v}_\mathrm{b}$ again, and we determine the angle θ between $\mathbf{v}_\mathrm{b}$ and $\mathbf{V}$. The angle distribution is presented in Fig.2.8d showing a decrease in the peak of the distribution. This "flattened" distribution confirms the importance of the flows near the glass in the propulsion of the droplet.

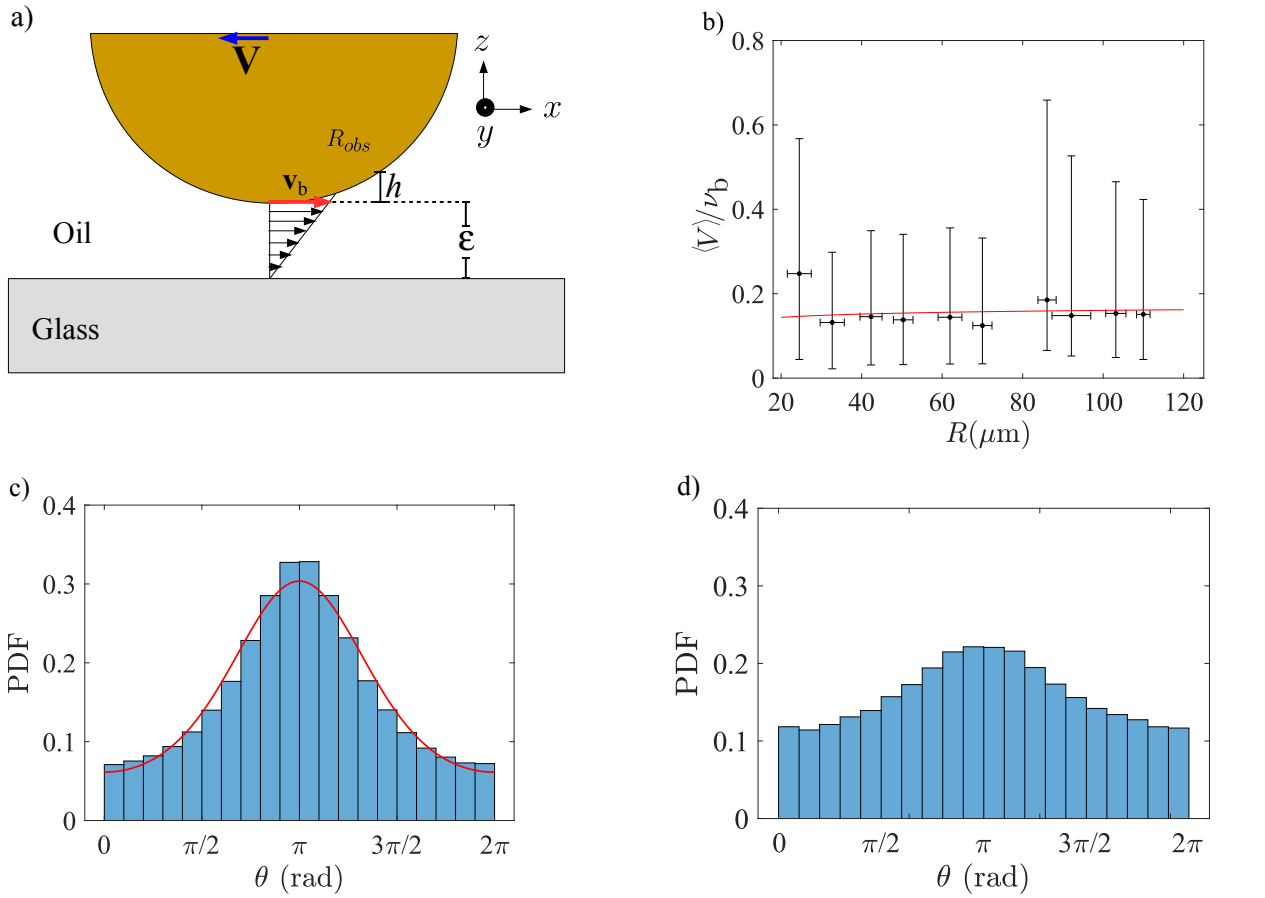

Figure 2.8: a) Schematics of the rolling with slipping of a drop. $\mathbf{v}_b$ is obtained averaging the velocity field in the observation region delimited by R_{obs} and averaged with the weight function w (eq. 2.4), which depends on the relative height to the bottom of the droplet h. The thickness of the lubrication film ε is shown out of scale for clarity. b) $\langle V \rangle / v_b$ as a function of drop radius R. Symbols represent experimental data, averaged over drops within windows of increasing radius in 10 µm increments. Horizontal error bars correspond to standard deviation on drop radius while vertical error bars represent the confident interval at 63%. Red curve corresponds to eq. (2.3) using $\varepsilon = 20$ nm estimated from Ref. [40]. c) Probability density function for the angle between $\mathbf{v}_b$ and $\mathbf{V}$. The red line is the fit for the von Mises distribution, eq. (2.6), showing a peak at $\theta = \pi$. d)Probability density function for the angle between $\mathbf{v}_b$ and $\mathbf{V}$ using the weight function from eq. (2.7), giving more importance to the outer part of the velocity field.

Chapter 3

Magnetic Controllable Motor

3.1 Methods and Protocols

3.1.1 Bacterial culture

Magnetotactic bacteria (*Magnetospirillum gryphiswaldense* MSR-1 strain) is used in this experiment, and, as it was explained in the introduction, these bacteria have an inner magnetic moment ($m \sim 10^{-16}$J/T), which allows them to swim along an external magnetic field. To start a culture (Appendix A.5), Hungate tubes are filled with 10 mL of *Flask Standard Medium* (FSM) (Appendix A.4). This medium is bubbled inside tubes with a gas containing 2% O_2 and 98% N_2. The tubes are then sealed and autoclaved. When the tubes are cooled to room temperature, each one is inoculated using a volume of 300 µL taken from a −80 °C stock (Appendix A.6). The culture is incubated in the absence of external magnetic field (just the Earth magnetic field is present) at 30 °C and 160 rpm between three or four days until it reaches an optical density (OD) 0.12 ± 0.02 measured at a wavelength of 600 nm. In such conditions, we got roughly 50% of north seekers (NS) and 50% south seekers (SS) in the suspension, consistent with a standard growth protocol of MSR-1 [45]. The culture is then centrifuged at 6000 rpm for 1 min. We remove the supernatant and add a little amount of FSM in order to have a dense bacterial suspension, ranging from $n \sim 10^8$ to 10^{11} bact/mL. Then, part of this suspension (~ 2 µL) is poured in hexadecane oil containing Span80 (2%-weight concentration) to prepare an emulsion by manual agitation.

3.1.2 Experimental Setup

Part of the emulsion (65 µL) is then placed inside a chamber composed of a double-sided tape adhered to a microscope slide, and sealed with a coverslip. The chamber has dimensions 1.5×1.6 cm and a height $H = 270$ µm. The emulsion is then visualized using a 40X objective (Zeiss A-Plan Ph2 Var2) and filmed at 25 fps with a Hammamatsu camera (ORCA Flash4 2048x2048 pixels) mounted on an inverted microscope (Zeiss AXIO Observer) adapted to

receive Helmholtz coils, which produce a uniform horizontal magnetic field $\vec{B}$ (Fig.3.1).

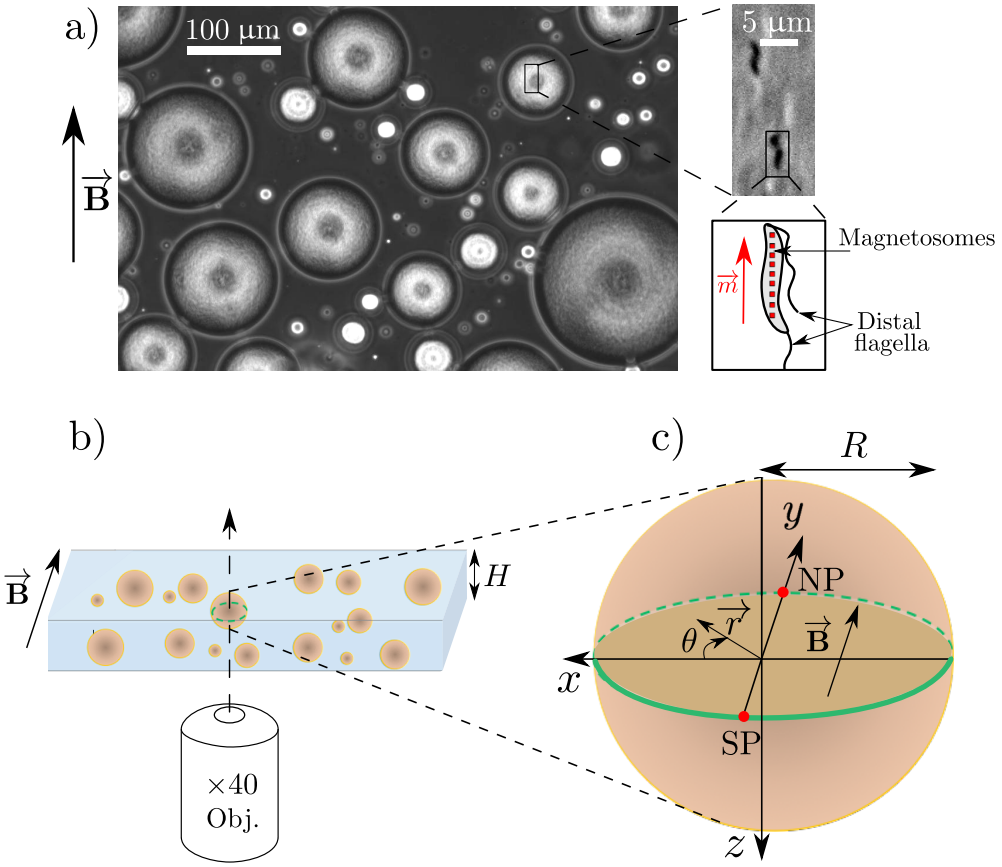

Figure 3.1: (a) ×10 phase-contrast image of an emulsion of magnetotactic bacteria (bacteria remain inside droplets) in hexadecane oil. A magnetic field of 4 mT is applied as indicated by the arrow. A broad distribution of droplets radii is obtained, spanning typically from 20 to 120 µm. *Zoom in:* ×40 phase-contrast image of two magnetotactic bacteria *Magnetospirillum gryphiswaldense* MSR-1 (darkest zones) swimming along the magnetic field direction. *Zoom in:* Sketch of a magnetotactic bacterium carrying magnetosomes (red squares) and two distal flagella. The magnetosomes are aligned along the body, generating a magnetic moment m. (b) Setup principle: a droplet, lying on the bottom plate of a pool of height $H = 270\,\mu$m and placed on the stage of an inverted microscope, is observed at its equatorial plane with a ×40 objective. A uniform magnetic field is applied in the observation plane, parallel to the bottom and top plates of the pool. (c) Definitions of the north pole (NP), the south pole (SP) of the droplet and the spatial coordinates. R is the droplet radius.

It is important to notice that the the magnetic field $\vec{B}$ lies in the (x, y) plane. The intensity of the magnetic field $B = |\vec{B}|$ is controlled electronically, from 0 to 4 mT. As a reference, the earth magnetic field has a value of $\sim 10^{-2}$mT and the first non-zero magnetic field used in our experiments is 0.2 mT, one order of magnitude bigger . Due to the low density of the hexadecane, droplets sediment at the bottom surface of the chamber. For all experiments, droplets sufficiently separated from each other (typically a distance of, at least, one droplet diameter) are observed. Also, experiments are always performed within 30 minutes after centrifugation for the largest concentration, because at longer times, bacteria show a decrease in

motility. Finally, for flow visualization outside the droplets, we used 1 µm-diameter melamine resin beads suspended in hexadecane oil.

3.1.3 Image analysis

PIV analysis

Before performing PIV on the images, they are treated subtracting the average-intensity image of the whole stack to every image (Fig.3.2). This allow us to get rid of the intensity gradients (which could lead to discrepancies in the flow measurement) inherent to both phase-contrast microscopy and PIVlab package for Matlab. After PIV is performed, the velocity field on a movie of typically 350 images (14 s) is averaged in time.

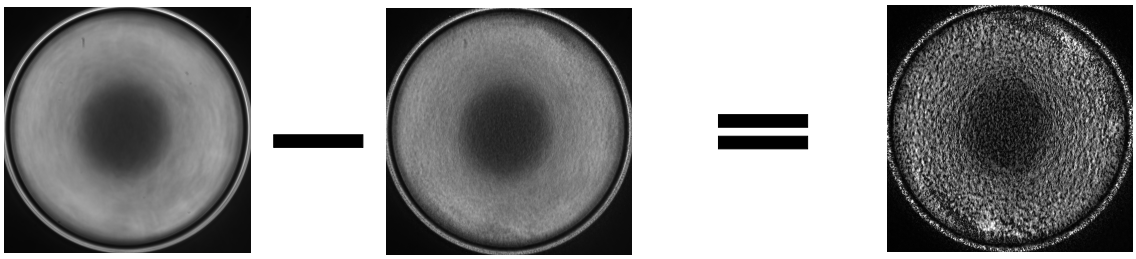

Figure 3.2: Example of difference between the average-intensity image (Left) and an image at a time t (Right). The resulting image is used to perform PIV.

Tracking analysis

Tracking of the 1 µm-diameter melamine resin beads suspended in hexadecane oil is performed by TrackMate plugin on Fiji (Fig.3.3). To smooth data, the velocity of each tracked particle on two successive images is averaged.

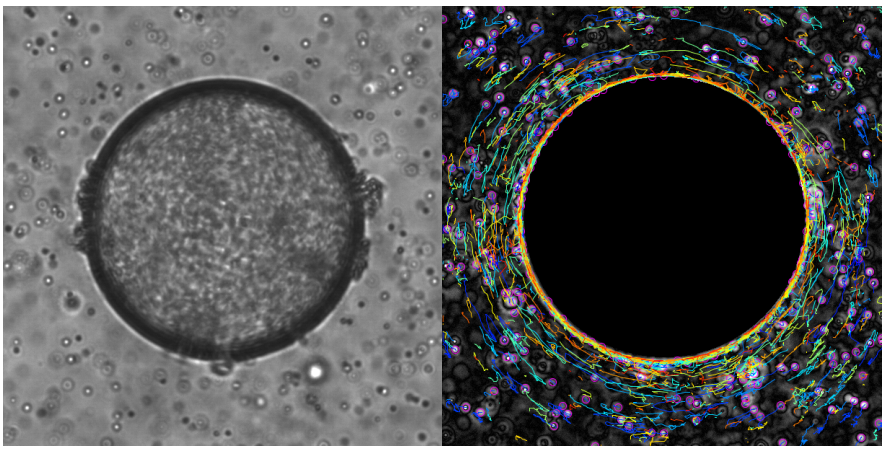

Figure 3.3: a) Example of tracking of 1 µm-diameter melamine resin beads suspended in hexadecane oil. In this case the droplet is encapsulating *E. coli*.

3.2 Results

3.2.1 Vortex flow inside the droplets

When the emulsion is poured inside the chamber, it is observed on the microscope and droplets are focused on their equatorial plane ($h = R/2$ measured from the bottom). In the absence of magnetic field, regardless of the bacteria density, the swimming direction of MTB in the drops is random and unbiased. When the suspension is dense, no large scale collective motion is observed. When a magnetic field is set in dilute conditions (for a cell density $n \sim 10^8$ bact/mL), NS (resp. SS) bacteria accumulate in the vicinity of the north (resp. south) poles of the droplet as a consequence of the bacteria swimming persistence described above (see Fig. 3.4 (a)). Because NS and SS bacteria are performing reversals, we observe some bacteria escaping from the accumulation regions. At an intermediate density (typically $n \sim 10^9$ bact/mL), the accumulation pattern becomes more unstable with episodic formation of jets propelling the fluid and the bacteria out of the polar positions, thus creating two local recirculation zones near each pole (see Fig. 3.4 (b)). For a dense suspension ($n \sim 10^{11}$ bact/mL), which is the case in the rest of the study, a steady and uniform collective rotational motion is observed, with an axis of rotation perpendicular to the magnetic field (see Fig. 3.4 (c)) and oriented along the gravity direction. Although all symmetric planes containing the magnetic field direction could have been chosen by the bacteria, the vortex is actually rotating in the x-y plane. This might be due to a sedimentation process (bacteria are about 20% denser than the medium [46]) which yields a stable stratified suspension. Visualization in other horizontal planes shows a similar rotation field as in the equatorial plane. The rotation direction chosen by the fluid is not completely random, with approximately 84% of the drops rotating in a clockwise (CW) direction looked from the top. This preferential choice of spontaneous rotation is not completely elucidated yet but may be related to the helicity of MTB. An interesting property of this collective rotational motion is that, regardless of the choice of rotation direction at the magnetic field onset, the direction can be reversed by reversing the magnetic field.

From now on, we focus on the characteristics of the vortex flow at a fixed density $n \sim 10^{11}$ bact/mL. For a magnetic field larger than a threshold value (typically 0.4 ± 0.1 mT), one observes the emergence of the large scale vortical flow previously mentioned. Through PIV analysis of phase-contrast microscopy images, we obtain the temporally and spatially resolved velocity fields due to the bacterial motion inside the drops $\vec{V}^{\mathrm{d}}(x, y)$ (Fig. 3.4 (d-e-f)). The flow field shows a central vortical structure and presents two maximal streams located near the poles reminiscent of the two jets visualized at lower bacterial concentration. The strength of the vortical flow field increases with the intensity of the magnetic field (Fig. 3.4 (e-f)). In the direction of the rotating motion, we also notice a shift of the bacterial accumulation with respect to the pole positions (identified by darker regions in phase-contrast images). For instance, for a CW rotation (as on Fig. 3.4 (e-f)), bacteria gather at the right of the NP and at the left of the SP in the (x, y) plane.

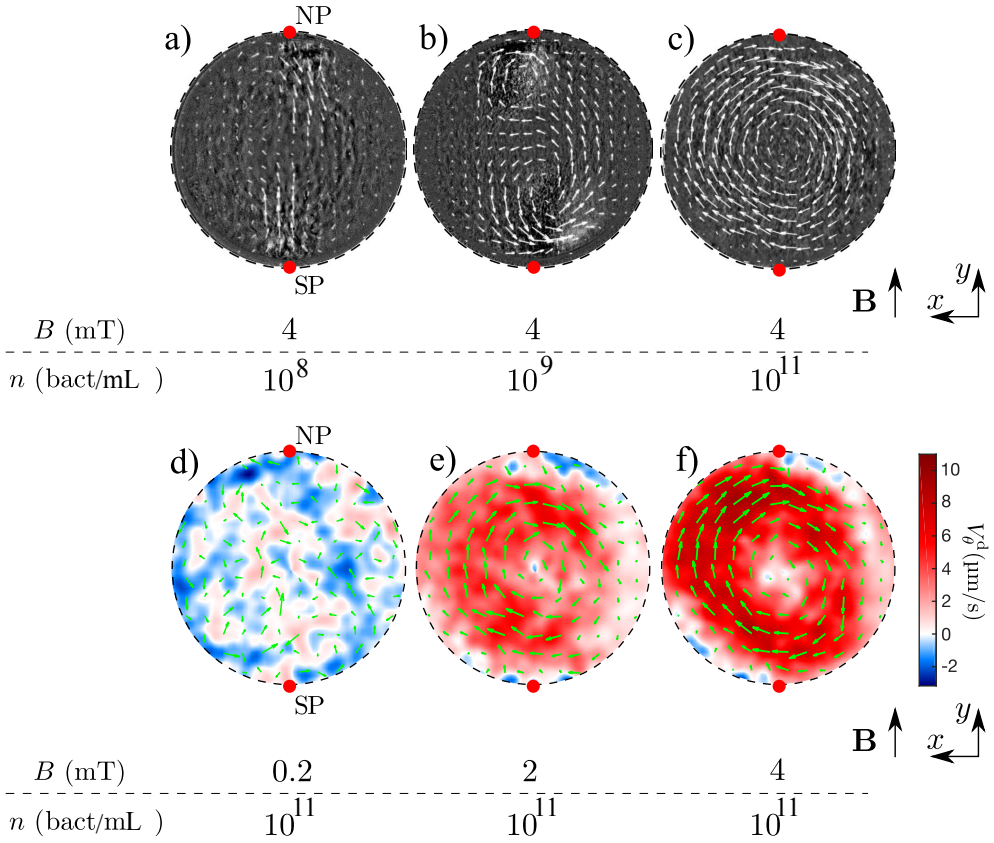

Figure 3.4: (a-b-c) ×40 phase-contrast images of droplets superimposed with time average PIV velocity fields (green arrows). We show the influence of the cell density n on the phenomenology, the magnetic field is fixed $B = 4\,\mathrm{mT}$. (a) $n \sim 10^8$ bact/mL, $R = 43\,\mu\mathrm{m}$: Bacteria accumulate at the poles of the droplet. (b) $n \sim 10^9$ bact/mL, $R = 89\,\mu\mathrm{m}$: unstable recirculation flows appear at the poles of the droplet. (c) $n \sim 10^{11}$ bact/mL, $R = 55\,\mu\mathrm{m}$: the bacteria self-organize to form a stable vortex flow at the center of the droplet. (d-e-f) Colored maps of the orthoradial projection of the instantaneous PIV velocity fields V_θ^d (red-blue colormap, enhancing positive and negative values) superimposed with the instantaneous PIV velocity field (green arrows). The radius of the droplet is constant $R = 83\,\mu\mathrm{m}$. We show the influence of the magnetic field magnitude on the phenomenology, the cell density is fixed $n = 10^{11}$ bact./mL. (d) $B = 0.2\,\mathrm{mT}$: no large scale collective motion is observed. (e) $B = 2\,\mathrm{mT}$: vortex flow centered at the droplet center. (f) $B = 4\,\mathrm{mT}$: the vortex flow is stronger than at $B = 2\,\mathrm{mT}$. (e-f) Recirculation flows (negative values of V_θ^d) close to the poles are identified in blue.

Computation of the angular average of the orthoradial velocity,

$$\overline{V_\theta^\mathrm{d}}(r) = \frac{1}{2\pi}\int_0^{2\pi} V_\theta^\mathrm{d}(r,\theta)\,\mathrm{d}\theta, \tag{3.1}$$

brings evidence for an effective solid-core rotating motion, characterized by an angular velocity Ω^d ($\overline{V_\theta^\mathrm{d}}(r) = \Omega^\mathrm{d} r$, see Fig. 3.5 (a)). The solid-core spans one-half of the droplet radius for all the radii investigated. At increasing magnetic field intensities, the magnitude of Ω^d increases to saturate at larger magnetic fields. Beyond the droplet core, the suspension is sheared and the velocity decreases down to a non-zero value at the droplet interface. PIV

analysis also shows that the accumulation of bacteria near the poles and at the droplet boundary, observed with phase-contrast images, correlates spatially with a local recirculation in a direction opposite to the core rotation (see blue regions enhanced in velocity maps on Fig. 3.4 (e-f)).

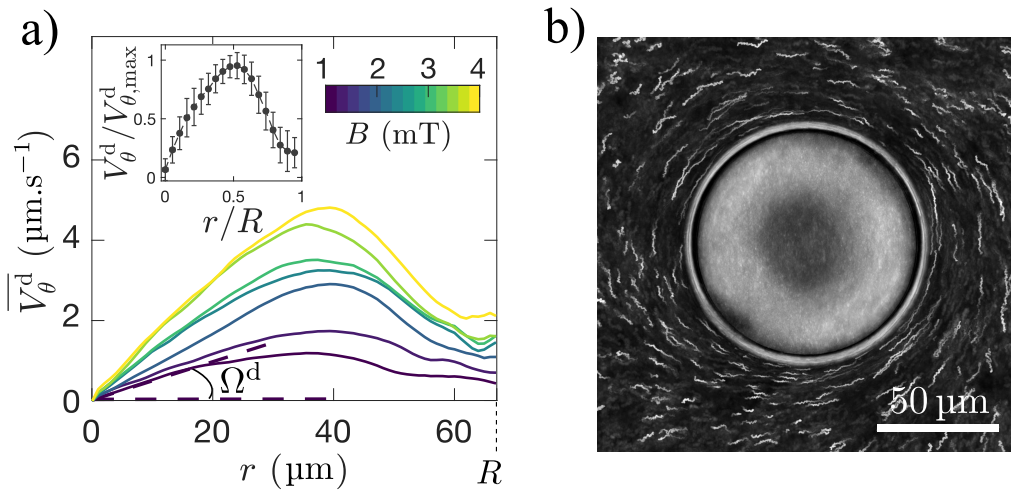

Figure 3.5: (a) Mean orthoradial velocity profile $\overline{V_\theta^{\rm d}}(r)$ for one droplet of radius $R = 67$ µm and for different magnetic field magnitudes B (colors, from bottom to top $B = 1$, 1.4, 2, 2.4, 3, 3.4, 4 mT). Close to the droplet core ($r = 0$), the suspension rotates like a solid with a characteristic rotational velocity $\Omega^{\rm d}$ which increases with B. Inset: Mean of the normalized curves. The errorbars are the standard errors. (b) Superposition of phase-contrast images (350 images corresponding to a 14 s movie) showing the circular rotation of the outer tracers for an inner rotational velocity $\Omega^{\rm d} = 0.13\,{\rm rad/s}$ measured at $B = 4\,{\rm mT}$.

3.2.2 Flow in the oily phase

To observe the flow of the surrounding hexadecane oil, we tracked 1 µm diameter melamine resin beads using TrackMate plugin of Fiji. The tracers, show a net circular flow (Fig.3.5b), which turns in the same direction as the central core rotation, but with local recirculation patterns opposed to the net fluid rotation, located close to the poles. These recirculation patterns mirror the previously mentioned counter-flow inside the droplet in Figure 2(e-f). Circulation of the velocity field

$$C(r,t) = \int_0^{2\pi} r V_\theta^{oil}(r,\theta){\rm d}\theta, \tag{3.2}$$

is computed on circles of several radii r centered on the droplet center at time t. Then, the circulation is averaged in time on the duration of the movie (typically 14 second) to get the mean circulation $\overline{C} = \langle C(r,t)\rangle_t$. Comparison of the circulation of tracers surrounding a droplet of *E.coli* shows no net circular flow, as the case of MTB (Fig.3.6). This net circular flow around MTB droplets, is evidence of a net torque applied on the surrounding hexadecane oil, which means that bacteria self assembly inside the droplet to form a rotary motor. Finally, the angular average of the orthoradial velocity, $\overline{V_\theta^{oil}}(r) = \overline{C}(r)/2\pi r$, is computed for different outer radii r for all droplets of different radii R and magnetic field B.

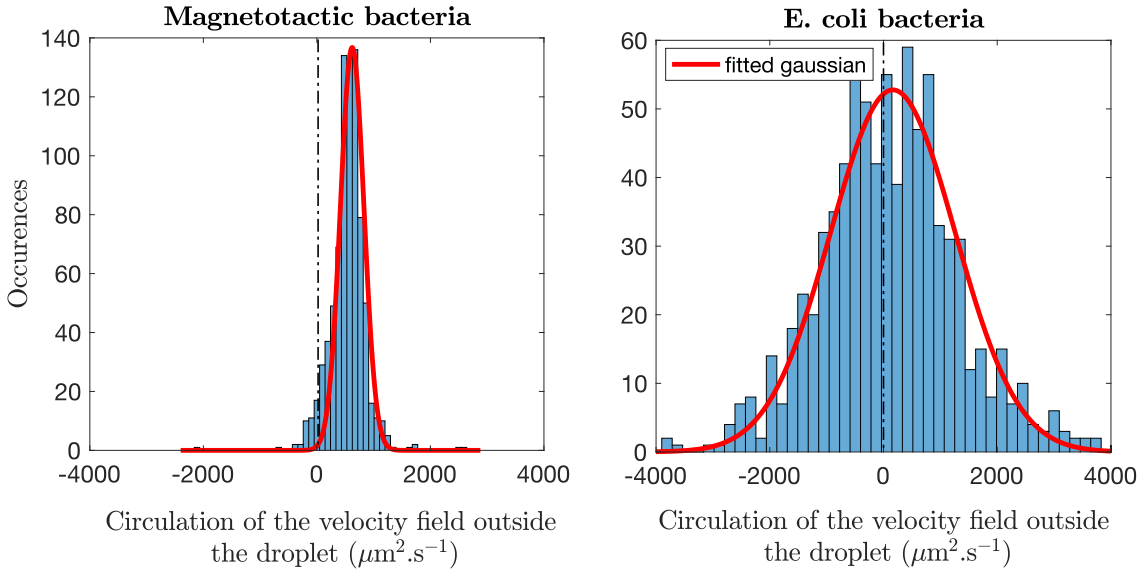

Figure 3.6: Comparison of the circulation around a droplet of MTB (Left) and *E. coli* (Right).

3.3 Discussion

3.3.1 Torque measurements

From the results, we propose that the inner droplet rotation is responsible for the net torque on the hexadecane oil. Now, we measure the energy production of the motor, namely, to measure the effective torque on the outer fluid, and we identify the mechanism of torque generation inside the droplet. The effective torque can be estimated by fitting the radial dependence of the mean orthoradial velocity, $\overline{V_\theta^{oil}}(r)$, with a simple hydrodynamic model, consisting in a sphere of radius R, driven in rotation by a torque τ and surrounded by an oil of viscosity η_{oil} (Fig.3.7a). As the droplet sits on the bottom plate of the chamber, the hydrodynamic image of the rotating droplet is needed, to account for the no-slip boundary condition of the flow field at the solid interface. So, the flow created by the rotating droplet, at a distance r to the center of the droplet at the equator of the drop is (for $r > R$)

$$\overline{V_\theta^{oil}}(r) = \frac{\tau}{8\pi\eta_{oil}R^2}\left[\frac{R^2}{r^2} - \frac{r/R}{(r^2/R^2+4)^{3/2}}\right], \tag{3.3}$$

where $\eta_{oil} = 3.47\,\mathrm{mPa\,s}$ is the dynamic viscosity of the hexadecane at 25 °C. The first contribution $\frac{R^2}{r^2}$ comes from the rotation of a sphere of radius R in the bulk, and the second part $-\frac{r/R}{(r^2/R^2+4)^{3/2}}$ is the contribution of the hydrodynamic image of the droplet, accounting for the presence of the bottom surface of the chamber. Using the experimental data of $\overline{V_\theta^{oil}}(r)$ (Fig. 3.7b), we obtain the torque τ for different radii and magnetic field. The dependence of τ with the angular velocity of the solid core inside the droplet, Ω^{d}, is shown in Figure 3.8a, where each point corresponds to an average over several droplets of similar radii. We observe an increase of τ with the radius and with Ω^{d}. Similarly, we present the dependence of the torque by unit volume $\tau_v = \tau/\left(\frac{4\pi R^3}{3}\right)$ with Ω^{d} in Figure 3.8b. A collapse of the points

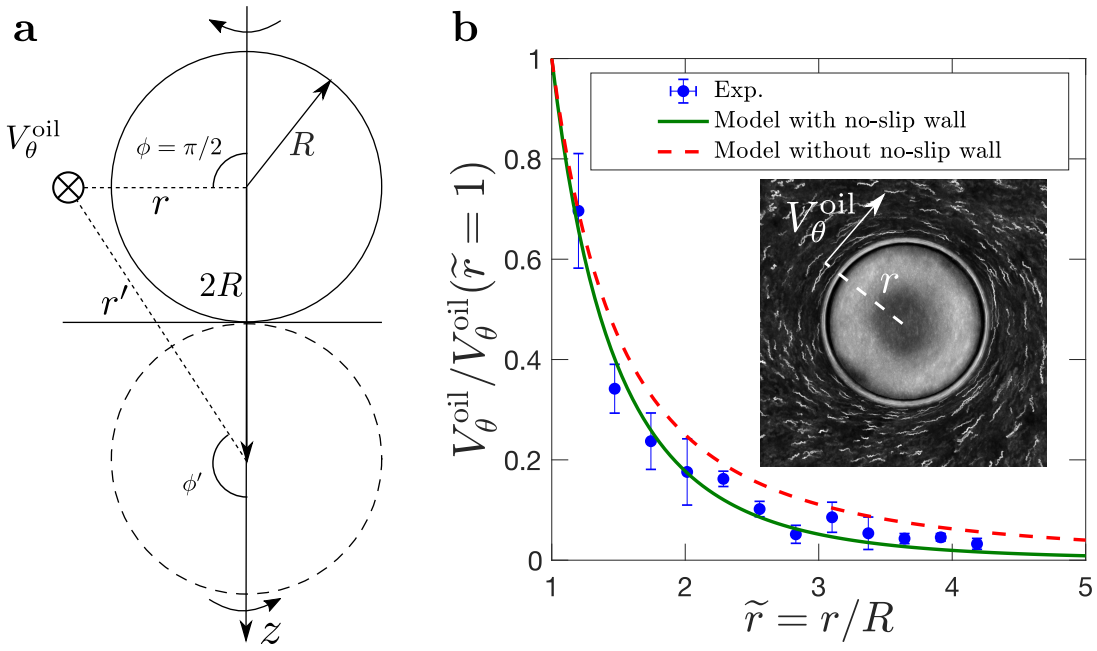

Figure 3.7: (a) Definition of the model and hydrodynamic correction due to the presence of the bottom plate of the pool. (b) Test of the hydrodynamic model on experimental data. Dotted line: model without corrective term accounting for the presence of the bottom plate. Solid line: model with corrective term.

onto an increasing curve is observed. This curve can be interpreted as the *operating curve* of the MTB droplet motor, analogous to the operating curve of macroscopic synchronous motors. It states clearly the dependence of the inner core rotation and the circular flow in the surrounding oil. The collapse of data shows that τ and Ω^{d} depend in a similar way with the radii and the magnetic field. The non-linear shape of this operating curve shows that the motor is less efficient at low Ω^{d} (typically for $\Omega^{\text{d}} = 0.05\,\text{rad/s}$) than at high Ω^{d}.

3.3.2 Mechanism of torque generation

As the resulting net torque on the surrounding oil is produced by force-free and torque-free swimmers, the only possible source is the misalignment of the magnetic moments of the MTB respect to the external magnetic field. The time that bacteria take to align with the external magnetic field, in a quiescent fluid, is $t_B = \xi_r/mB$, where $\xi_r = \pi\eta_w l^3/3\log(2l/a)$ is the rotational friction coefficient, $l = 3-4\,\mu\text{m}$ is the body length of one bacterium, $a = 1\,\mu\text{m}$ the body width, and $\eta_w = 1.00\,\text{mPa s}$ is the dynamic viscosity of water. Using these typical values, and for a magnetic field of $B = 2\,\text{mT}$, we get $t_B \approx 0.1\,\text{s}$. Inside the droplets, bacteria are forced to turn in order to align and swim along the interface. The alignment time with the boundary can be estimated as $t_T = l/V_0$, and using the typical values for the MTB yields $t_T \approx 0.1\,\text{s}$, which is the same order of magnitude as t_B. Hence, the droplet boundary makes the bacteria at the interface misaligned with the magnetic field, which leads to the generation of torque in the droplet. The misalignment of bacteria changes according to the position near the interface inside the droplet. The maximum misalignment is more likely at the poles (north and south), where the boundary is perpendicular to the magnetic field

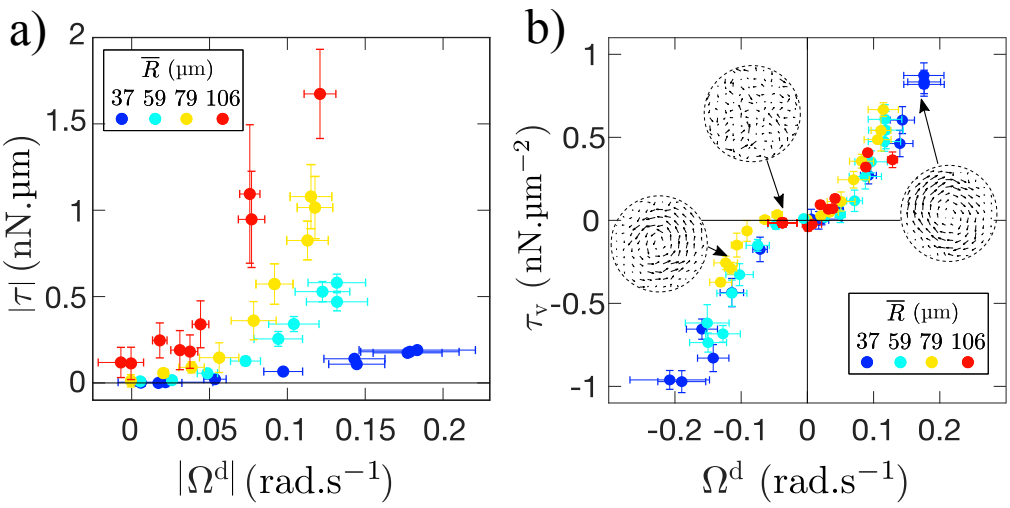

Figure 3.8: (c) The torque τ, acting on the oil and produced by the droplets, is extracted from the tracers orthoradial velocities (see (b)). We measure $\tau(B, R)$ for different droplets radii R and magnetic field B with respect to the core rotation velocity $\Omega^d(B, R)$ (average data for 10 droplets of similar radii, $\overline{R}$ is indicated by colors and is given with a ± 15 µm standard deviation). The errorbars are $\sigma/\sqrt{N}$ where σ is the standard deviation and $N = 10$ (number of droplets used for the average). (d) Torque by unit volume $\tau_v = \tau/(\frac{4}{3}\pi R^3)$ as a function of Ω^d for the same data set. The average data for different $\overline{R}$ collapse on the operating curve of the rotary motor. The velocity maps are the ones of the droplet displayed on Fig. 3.4 (d-e-f) and placed at the corresponding operating points.

direction. The kinematics happening inside the droplet is now explained taking as an example a droplet rotating CW without loss of generality. In this case, due to the advection by the central vortex core and their swimming propulsion along the magnetic field direction, NS and SS bacteria reach the droplet boundary and align with it, in the case of the NS, at the right of the north pole, and for the SS at the left of south pole, everything occurring in the $x - y$ plane. The magnetic torque on those misaligned bacteria (both at the NP and SP) points in the CW direction, reinforcing the circulation. As NS bacteria swim along the droplet boundary, their misalignment with $\overrightarrow{B}$ increases while they are getting close to the north pole (south pole for SS bacteria), until the magnetic torque becomes too large to be compensated by the boundary alignment. Then, the bacteria leave the droplet boundary causing a release of the magnetic torque in the fluid. Further on, they align back along the magnetic field and are advected by the vortical flow, before reaching back the droplet boundary and closing the loop. The picture described above, is consistent with the counter-rotating flows observed inside and outside the droplet. The time-scale analysis allow us to infer that the bacteria misaligned on the interface are responsible for the torque generation. This points to a surface effect, and we can state

$$\tau = n\mathcal{V}mB, \tag{3.4}$$

where, $\mathcal{V}$ is the volume of bacteria contributing effectively to the torque. The dependence of this volume with the radius is expected to be $\mathcal{V} \sim \lambda R^2$ to account for the surface effect, where λ is a typical length independent of R. Computation of $\lambda = \tau/nR^2mB$ (Fig.3.9) shows a collapse of all data, in average, on a constant curve with $\lambda = 8 \pm 2$ µm, which confirms that λ does not depend neither on the magnetic field intensity nor on the droplet radius. Besides,

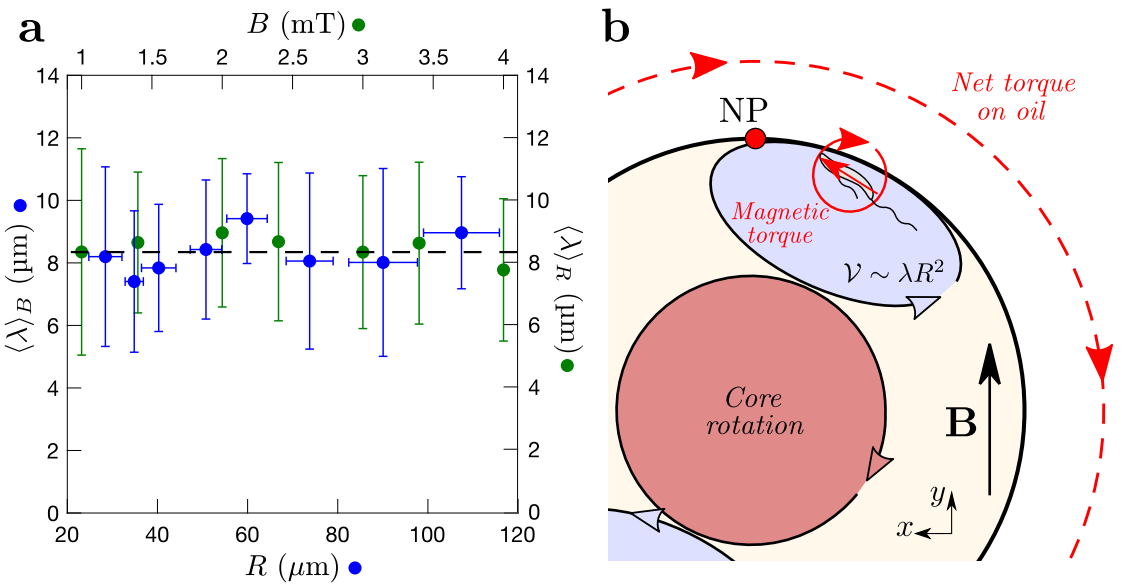

Figure 3.9: Test of the scaling relation $\tau = nmB\lambda(R,B)R^2$ where τ is the generated torque, $n \sim 10^{17}$ bact/m^3 is the bacteria density, $m \sim 10^{-16}$ J/T is the magnetic moment of a single bacterium, B is the magnetic field intensity and $\lambda(R,B)$ is a typical length inherent to the torque generation. (a) $\langle\lambda\rangle_B$ (resp. $\langle\lambda\rangle_R$) is the average value of λ with respect to B (resp. R). We only included the data corresponding to $\tau_v > 0.2$ nN/μm^2, for which the torque is strong enough to be measured out from experimental noise. The error bars are the standard deviations of the average data. This graph shows that $\lambda = 8 \pm 2$ μm is an intrinsic length of the system which does not depend on R nor B. (b) Qualitative interpretation of the rotary motor self-organization. The volume of the recirculating bacteria contributing to the torque is dimensionally $\mathcal{V} \sim \lambda R^2$. The picture is similar close to the south pole of the droplet.

λ is of the order of a bacterium size, and can be related to a microscopic scale, consistent with no dependence on both, R and B. Thus, the picture emerging from our scaling analysis is that of one core rotation and two counter-rotating regions made of self-assembling bacteria at the poles and yielding a net torque to the oil (Fig.3.9).

3.3.3 Vortex reversal

Using the description mentioned above, of the mechanism of torque generation, we are now able to give an explanation to the vortex reversal, performed by the switch of the magnetic field. When the magnetic field is rapidly reversed, the bacteria that are accumulated at the right of the north pole and at the left of the south pole can suddenly rotate to align along the new magnetic field. Then, they cross the droplet roughly in the y-direction, which is consistent with positive values of Ω^{d} (corresponding to CW direction) measured just after the magnetic field reversal (Fig.3.10a). After crossing the droplet, they accumulate near the new north and south poles, which are located on opposite positions to the original ones. Thus, the MTB that were accumulated CW of their respective poles are now CCW of the new poles and, hence, generate an opposite torque provoking the inversion of the motor (Fig.3.10b). As we mentioned at the beginning of this chapter, there is a natural tendency to create a CW motor,

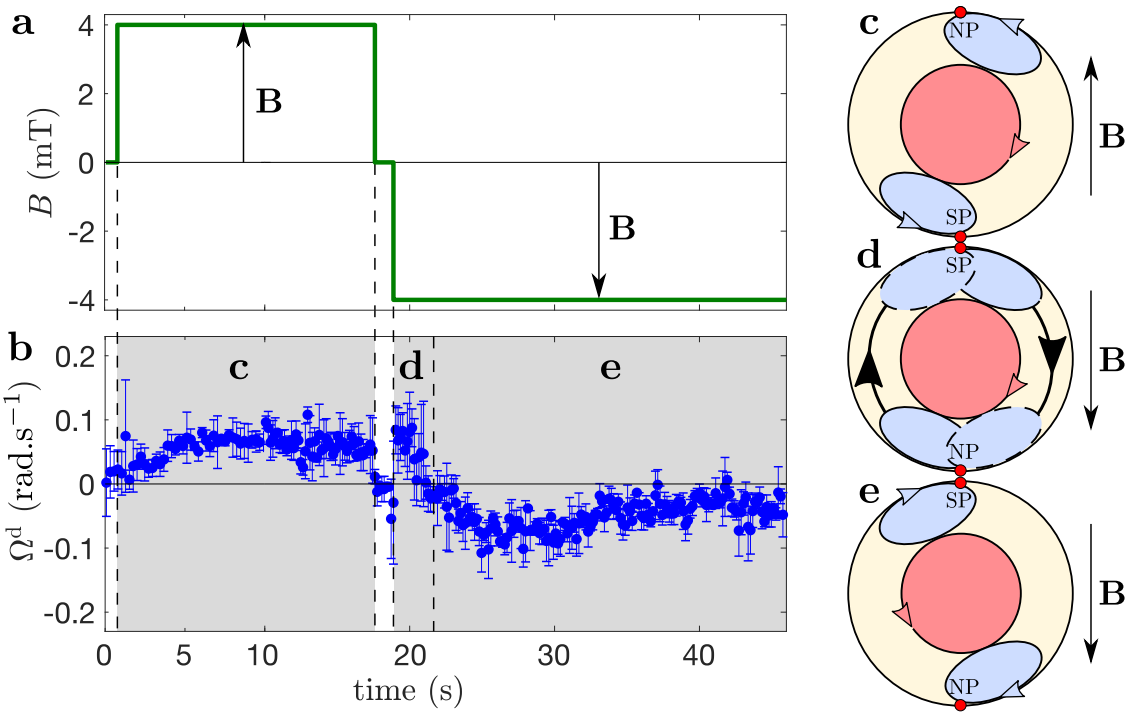

Figure 3.10: Top: magnetic field amplitude B as a function of time. Bottom: response in the rotational velocity of the droplet core Ω^{d} under the applied magnetic field. (c), (d) and (e) are the stages corresponding to the particular self-assemblies representations on the sketches on the right of the figure. The coral region corresponds to the central core rotation while the blue zones represent the recirculating bacteria. The bacterial suspension is dense ($n \sim 10^{17}$ bact/m^3). For each time step t, $\Omega^{\mathrm{d}}(t)$ is computed from instantaneous PIV maps as in Fig. 3.5 (a). From the moment when the magnetic field is set, Ω^{d} reaches a stationary value within a few seconds ($\sim$4 s). When reversing quickly the magnetic field direction while the suspension rotates CW, the suspension continues rotating CW at the short times after reversal before reversing completely its rotational direction to CCW. Then, Ω^{d} reaches a stable negative value $\sim$10 s after the magnetic field switch.

so in order to make this mechanism efficient, the time duration between the application of the two opposite magnetic fields must be shorter than the thermal reorientation time, which is of the order of the inverse rotational diffusion constant $D_r = 1/80\,\mathrm{s}^{-1}$, as presented in Figure 3.10. If the switch reversing the magnetic field takes longer, the MTB have time to reorient isotropically and leave the accumulation zones.

Chapter 4

Bacterial Shells

4.1 Methods and Protocols

4.1.1 Bacterial culture

We use *E.coli* run and tumble strain RP437, which contains a plasmid to express the green fluorescence protein (GFP). The stain is collected from a $-20\,^{\circ}\mathrm{C}$ stock, and grown about 24 h at $30\,^{\circ}\mathrm{C}$ with an agitation of 200 rpm in 10 mL of M9G medium (Appendix A.9) plus 10 µL of Chloramphenicol (CAM). The next day, the suspension is harvested in the exponential phase of the growth curve when it reaches an optical density (OD) of 0.5 measured at a wavelength of 600 nm. Then, six tubes, each one with 10mL of bacterial suspension, are centrifuged at 5000 rpm for 7 min. After centrifugation, supernatant of each tube is removed, letting a little amount ($\sim$ 1 mL) to resuspend the pellet. Now, all the resuspended pellets are gathered together in one single tube, which is centrifuged again at 5000 rpm for 7 min. The supernatant is removed completely this time, letting the pellet alone, and 100 µL of a phosphate motility buffer (Appendix A.8) with 3% in weight of polyvinyl alcohol (PVA) is added to finally resuspend the pellet. The phosphate motility buffer is a minimal media, where bacteria can swim but do not divide. With this protocol we obtain a volume of $\sim 100\,\mu\mathrm{L}$ of a dense suspension with a bacterial concentration $n \sim 1.5 \times 10^9$ bact/mL. Some remarks regarding this protocol, explaining why is different from Chapter 2 is explained in Appendix A.12.

4.1.2 Experimental Setup

The device used to make the bacterial shells, where a drop is placed inside a drop, is the one in Figure 4.1. It consists of three glass tubes: inlet, square and outlet capillary. The liquids passing through these tubes, following the same order, are called inner, middle and outer fluid. The injection of the middle and outer fluid is done at the square capillary, while the inner fluid is injected directly at the inlet capillary. The three fluid phases interact in

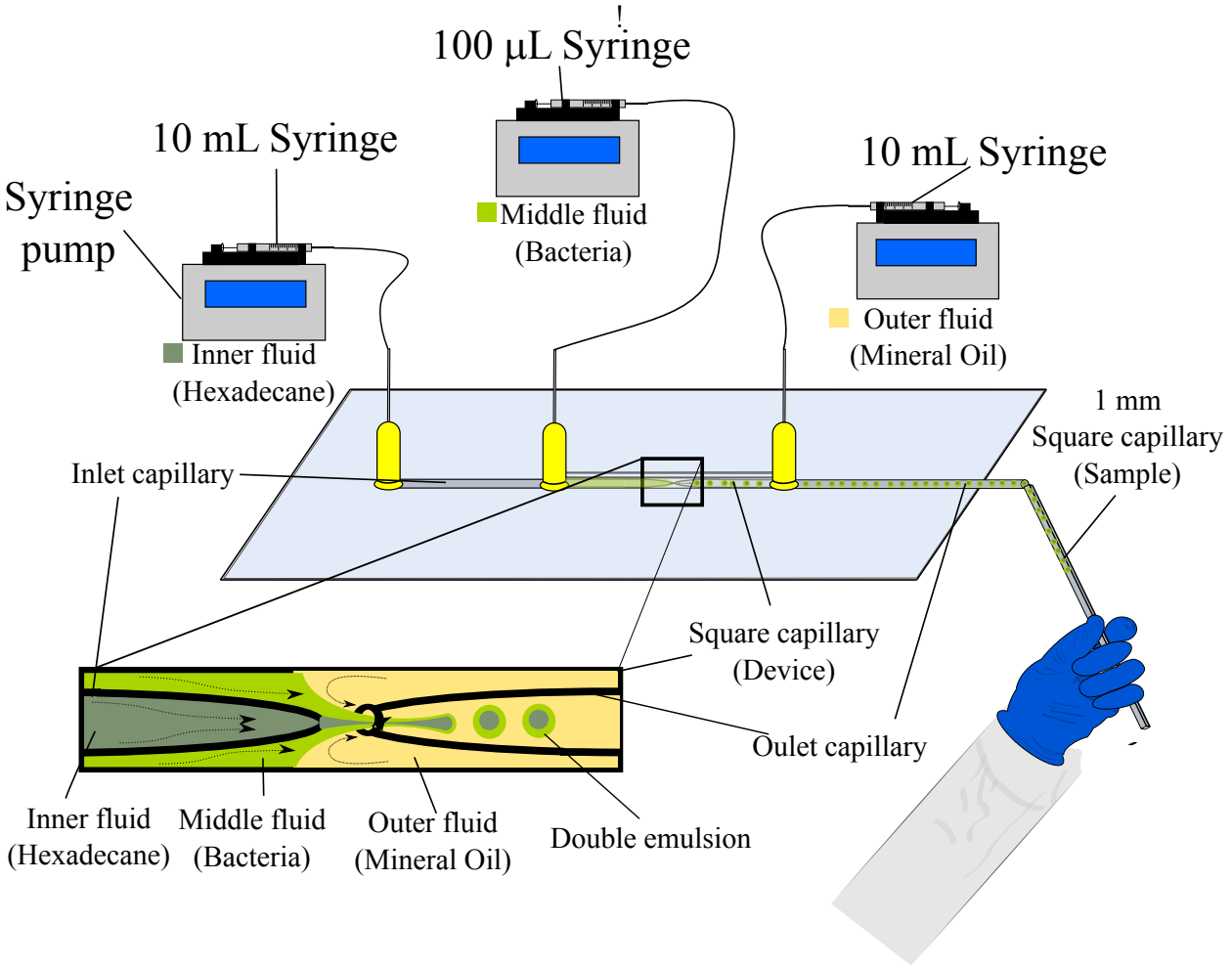

Figure 4.1: Double emulsion setup

the space between the two round capillaries (inlet and outlet), and the outer fluid is the responsible to drag the other two fluids (inner and middle) into the outlet capillary, where the shell forms obtaining a double emulsion. This device is mainly used for preparing water in oil in water emulsions (W/O/W). Our objective is to make a bacterial shell, so it must be an oil in water in oil emulsion (O/W/O). As no protocols existed in this case, the first part of this work was dedicated to find the good fluids in order to obtain the O/W/O emulsion using a biocompatible aqueous phase. The resulting protocol we created is described in the following.

A 10 mL Hamilton syringe with a 2 µm filter containing Hexadecane with Span 80 as a surfactant (2% weight) is connected to the inlet as inner fluid, while the bacterial suspension placed inside a 100 µL Hamilton syringe is connected to the square capillary as middle fluid (without filter), and finally a 10 mL Hamilton syringe with a 2 µm filter containing Mineral oil with Span 80 as a surfactant (2% weight) is connected also to the square capillary as outer fluid. With this configuration we obtain a water in oil droplet, with an oil droplet inside the water phase, and this device creates drops of radii between $\sim$ 20 to 150 µm for the outer drop (bacterial drop) and radii of $\sim$ 5 to 100 µm for the inner drop (hexadecane drop).

The syringes are connected by tubing to the device and the flows are controlled by syringe pumps. The double emulsion formation is observed by means of a Phantom camera filming at 16000 fps mounted on a Nikon inverted microscope and using a 10X objective. When the emulsion is made, it is collected into a 1 mm square capillary and observed using an inverted confocal microscope with a 40X objective in bright field of fluorescence, filming at 25 fps or 50 fps with a Hammamatsu camera mounted on the microscope. Besides, the confocal microscope can be rotated, which allows us to observe the drops from the side instead of the top-bottom sight. Videos of double emulsion in the horizontal plane were recorded with an upright Nikon microscope. In the following, we refer as R_{out} to the radius of the bacterial drop, and R_{in} to the inner hexadecane droplet (Fig. 4.2)

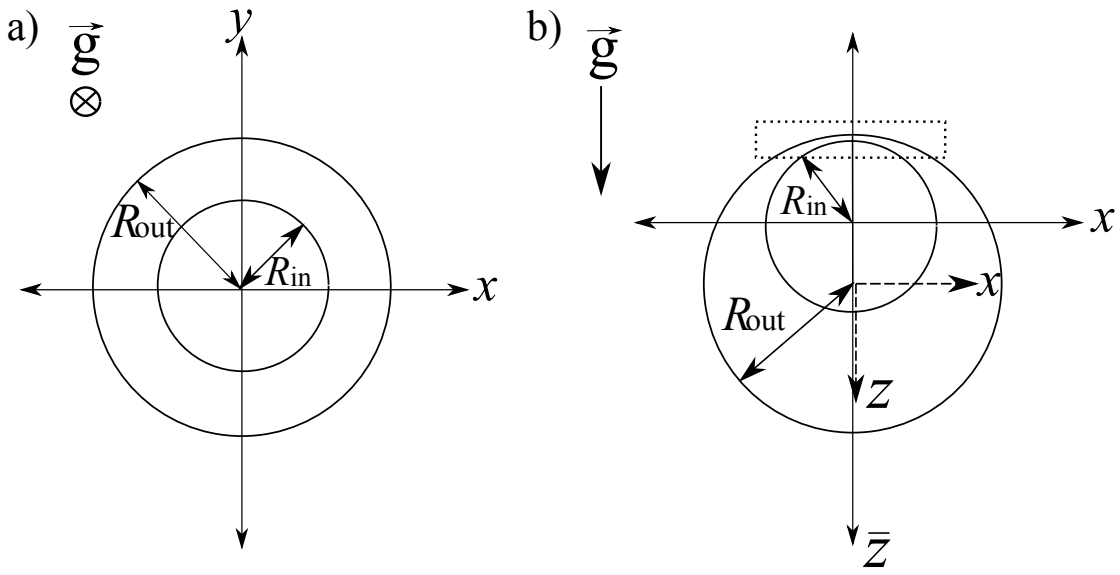

Figure 4.2: Coordinates defined on the double emulsion. a) Horizontal plane. Gravity is entering the page. The inner circle is the hexadecane droplet, while the external circle is the bacterial drop. b) Vertical plane. The axis with the dashed line are defined on the center of the bacterial drop. The solid line axis is defined at the top position of the inner hexadecane droplet. The dotted lines encloses the top region of the shell, where there is a thin film of bacterial suspension, preventing the hexadecane droplet to touch the bacterial drop interface. The positive direction of the coordinate system is labeled with the x and $z(\overline{z})$ letter.

4.1.3 Image analysis

PIV analysis

In the case of big inner droplets ($R_{\text{in}} \geq R_{\text{out}}/2$), there is a thin layer of bacteria swimming between the interface of both droplets at the top (Fig.4.2b) dotted line). Observing the sample in a horizontal plane this thin layer of the double emulsion is recorded, using a Nikon camera, with a 40X objective mounted on a Nikon upright microscope. The velocity field is obtained using the PIVlab Matlab package to perform PIV on the images, which are previously treated in the same way than the magnetotactic droplets, subtracting the resulting average-intensity image from the whole stack to each image (Fig.4.3). The duration of the recorded movies to perform PIV in the horizontal plane is typically of 250 images (10 s).

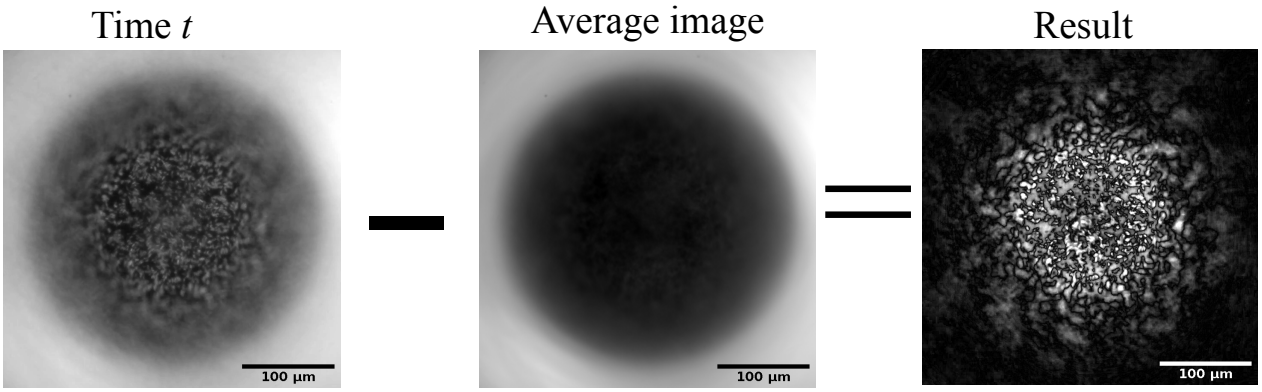

Figure 4.3: Example of the difference between the average image and an image at a time t. The image is in the horizontal plane, and focused on the top of the shell where it is observed the thin layer of bacteria. The hexadecane drop is right below forming this layer.

Tracking

When the inner hexadecane droplet is $R_{\text{in}} \leq R_{\text{out}}/2$, it moves randomly inside the bacterial drop. Besides, the bacterial drop may change sometimes its position as well. In order to obtain the position of both droplets, a matlab code was developed, using the function *imfindcircles*, similar to the one in Chapter 2 (Fig.4.4). The code reads the camera video format (.MOV,.cxd and .nd2), and looks for two droplets of the desired radius, cropping automatically the image around the big droplet. The code compares the found circles in the current image, to the ones found in the previous image to correct the positions of both droplets. If no drops are found, the sensibility of the *imfindcircles* increases until finding circles and compares them again with the circles found in the previous image. After the tracking process, the tracks are smoothed averaging over 10 points. Then, the data is ready for analysis.

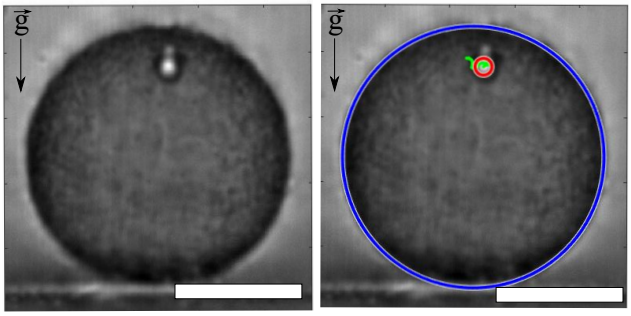

Figure 4.4: Example of tracking of the double emulsion. Both drops are detected, and the green points are the trajectory performed by the little droplet over the last 100 frames. Scale bar 30 µm

4.2 Experimental Results

4.2.1 Double emulsion

Depending on the flow rate, each shell of the double emulsion can be formed by just one or several hexadecane droplets inside the bacterial suspension (Fig.4.5). In our case, we aim to have a single hexadecane droplet inside the aqueous drop. In Table 4.1 there are examples of flow rates that we found for the production of a single droplet inside. The first column corresponds to a big inner droplet ($R_{\text{in}} \geq R_{\text{out}}/2$), and the second column to a little inner droplet ($R_{\text{in}} \leq R_{\text{out}}/2$).

	Flows µL/h	Flows µL/h
Inner:	800	2000
Middle:	800	800
Outer:	5000	5000

Table 4.1: Examples of flow rates imposed by the syringe pumps for double emulsion production. Left column: Production a big inner droplet ($R_{\text{in}} \geq R_{\text{out}}/2$). Right column: Production of a little inner droplet ($R_{\text{in}} \leq R_{\text{out}}/2$).

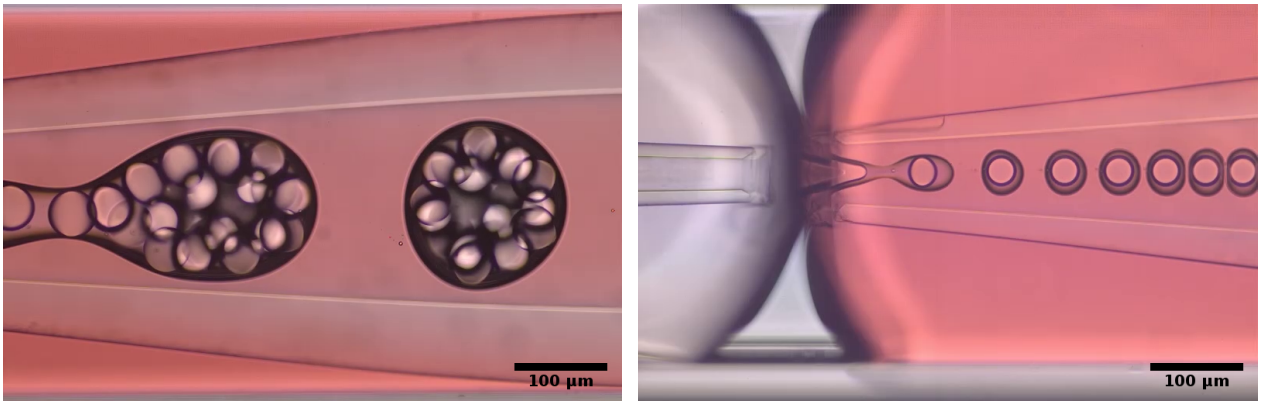

Figure 4.5: Example of double emulsion production.

It is important to say that they are just reference values, because the device is very sensible, and the exact values may change from other devices built with the same parameters and in the same conditions. After production, the double emulsion can be stable for hours, but bacteria swim keeping the same activity just within the first 30 min approximately, which limits the available time to perform experiments. Due to the density difference between mineral oil, water, and hexadecane, the inner droplet ascends, while the whole bacterial drop sediments to the bottom of the sample (square capillary). This means that the upper part of the shell has a thin layer, while the bottom has more space. This can be seen using the rotating confocal microscope, where the sample is tilted in 90° and we can confirm the position of the hexadecane droplet (Fig.4.6). Another interesting result regarding the double emulsion formation, is that it can be achieved following the protocol of Chapter 2 for bacterial droplets, with the difference that in order to form the double emulsion the fluids must be shaken much stronger. This method does not work in all cases, and one must look for individual shells between several bacterial droplets, and there is no control on the droplet size, neither on the inner nor on the outer drop of the shell.

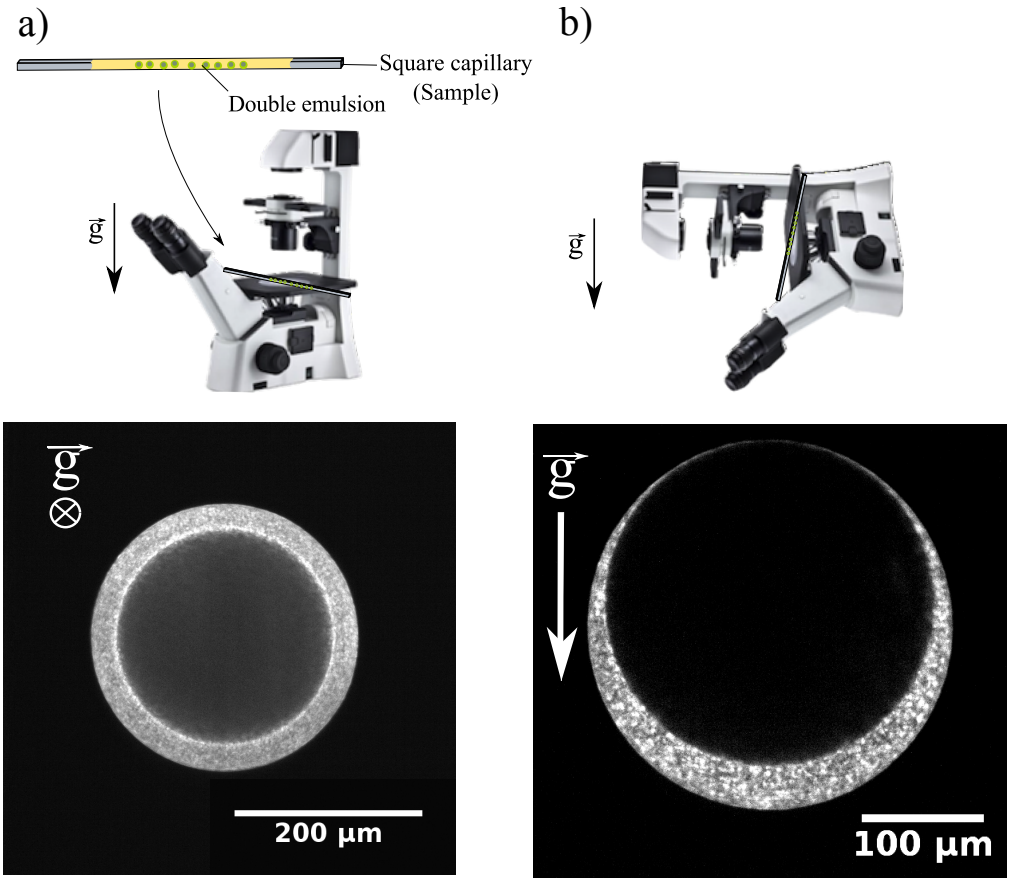

Figure 4.6: Observation of double emulsion in a confocal microscope with a 40x objective. a): Observation in the horizontal plane. The image is in fluorescence, showing the bacterial suspension (bright ring), the inner hexadecane droplet (black inner circle) and the mineral oil (black background). b): Rotation of the microscope in 90° showing a different shell from a). Since hexadecane is less dense than the bacterial suspension, the inner hexadecane droplet locates at the top of the bacterial shell

4.2.2 Collective motion

When $R_{in} \geq R_{out}/2$, simple inspection of the thin layer of the bacterial shell shows bacteria moving in several well defined vortices. The correlation length of the velocity field $\mathbf{v}(x, y, t)$ (Fig.4.7) is computed in time, and the minimum of the correlation is averaged in time over the whole video (10 s). The resulting correlation length was averaged for 11 different shells showing a typical size of 37 µm. Also the correlation time was computed, showing in average a typical duration of the vortex of 0.26 s, consistent with the typical persistence time found for the dense suspension in Chapter 2. New experiments recording longer times (e.g. 20 min) can shed light on the interesting dynamics happening in this part of the bacterial shell.

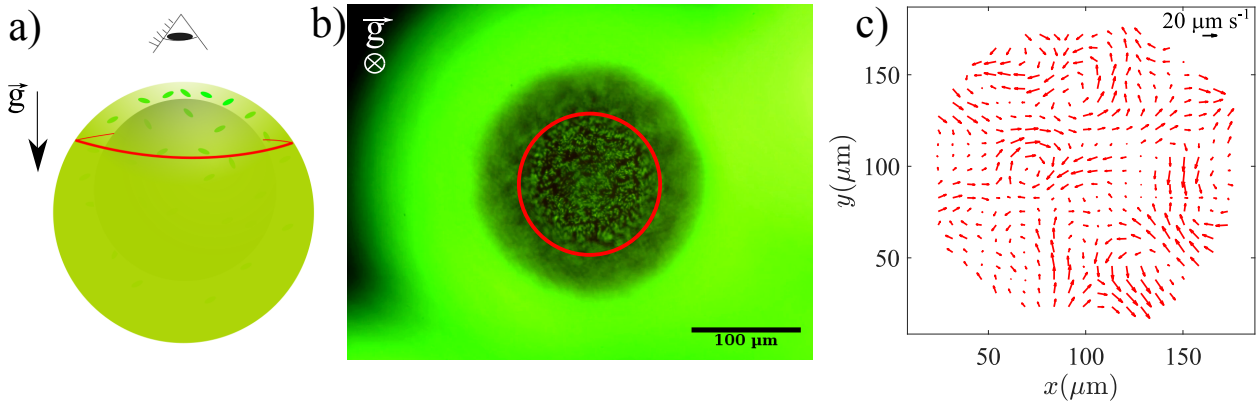

Figure 4.7: a) Schematic of a bacterial shell with a big inner drop. b): Fluorescence image taken with a 40X objective. c): Example of an instantaneous velocity field measured using PIV within the red circle drawn in a) and b)

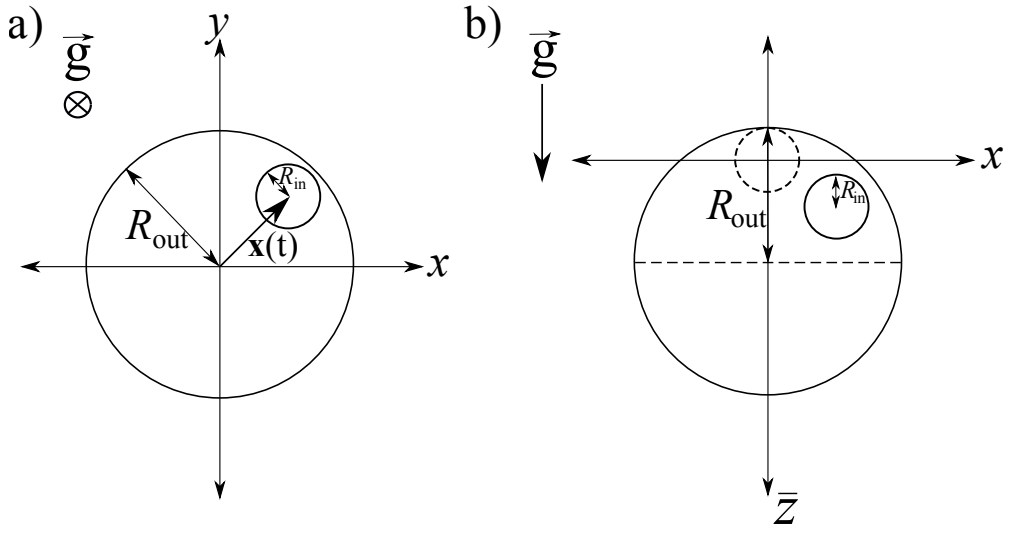

Figure 4.8: Coordinates defined on the double emulsion in the case of a little hexadecane droplet ($R_{in} \leq R_{out}/2$). a) Schematics showing the instantaneous position $\mathbf{x}(t)$ of the inner hexadecane droplet respect to the center of the bacterial drop. b) The same example in a) but in the vertical plane. The dashed circle represents the minimum position of the inner droplet at the top. The dashed line traverses the center of the bacterial drop.

4.2.3 Droplet random walk

Random movement of the inner hexadecane droplet is observed when $R_{\text{in}} \leq R_{\text{out}}/2$ (Fig.4.8). Drops were recorded horizontally and another set of experiments was performed with the sample tilted 90° to study this random movement against gravity. In the $x-y$ plane, the position of the hexadecane droplet $\mathbf{x}(t)$ is measured from the center of the bacterial drop. In the case of z coordinate, we define a new coordinate $\bar{z}$ starting from the top of the drop and increasing positively to the center of the drop, that is, $\bar{z} = z - R$ where $R = R_{\text{out}} - R_{\text{in}}$ considering the minimum position of the inner hexadecane droplet (Fig.4.8). The mean square displacement (MSD) is computed (Fig.4.9), revealing a persistent random walk. Thus, the ballistic part for short times and the diffusive part for intermediate times are clearly seen, but no plateau due to confinement is observed because of the insufficient recorded time. The same equation for the bacterial droplets in Chapter 2 to fit the MSD is applied (Eq.2.1), showing in average a persistence time of 0.28 s and a diffusion coefficient that depends on the size of the small droplet both for displacement in the horizontal and vertical plane (Fig. 4.10). In the case of the horizontal plane, we fit the diffusion coefficient by a linear model (red line Figure 4.10), $D = D_0 + D_1 R_{\text{in}}^{-1}$ where $D_1 = 21.48 \pm 8.5\,\mu\text{m}^3/\text{s}$ and $D_0 = 0.0035 \pm 0.5\,\mu\text{m}^2/\text{s}$. The exploration performed by the inner hexadecane droplet in the horizontal plane is apparently isotropic (Fig.4.11 a)), while the movement in z tends to be concentrated near the top due to buoyancy (Fig.4.10 b) Fig.4.11 b)).

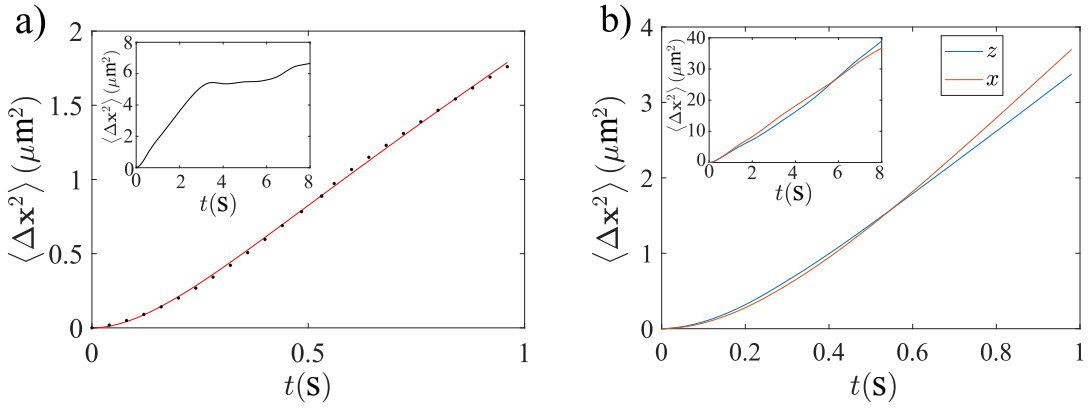

Figure 4.9: Example of MSD. The ballistic and diffusive part are clearly seen, but the saturation due to the confinement is not clear (Inset). a) MSD in the horizontal plane. Black dots are experimental data, and the red line is the fitting of equation 2.1 with R-squared 0.99 b) MSD in the vertical plane.

4.3 Discussion

The fluctuations for the position of the inner droplet, can be understood as a result of an active temperature of a *bacterial gas*. A first approach to compute this active temperature is by means of the diffusion coefficient. As can be noticed from Fig.4.10, the diffusion coefficient in the $x-y$ plane depends on the inverse of the radius, and it can be compared with the

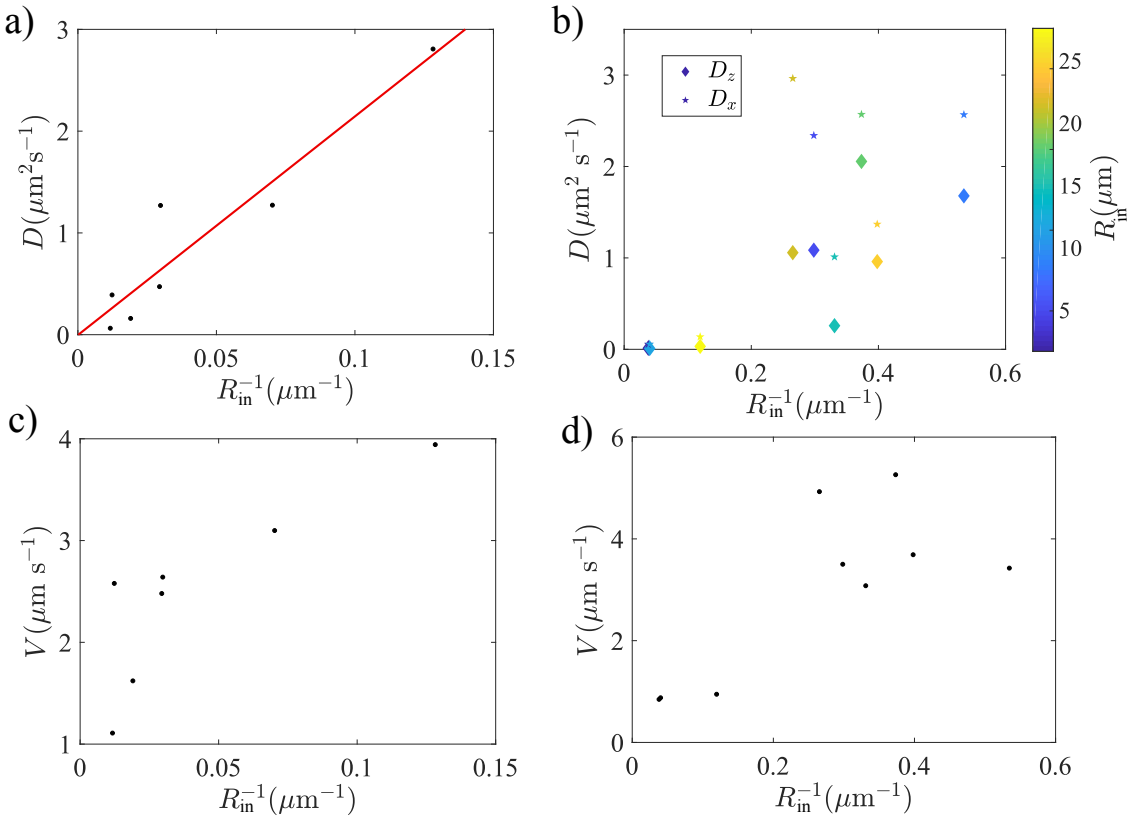

Figure 4.10: Diffusion coefficient and mean speed for the inner hexadecane droplet. a) Diffusion coefficient in the horizontal plane. Red line is a linear fitting with R-squared 0.91 b) Diffusion coefficient in the vertical $x-z$ plane. Note that the diffusion coefficient is presented separately for the x and z axis. c) Mean speed in the horizontal plane. d) Mean speed in the vertical plane.

thermal diffusion coefficient using the factor in Eq.2.2 yielding

$$T_{\text{active}} = \frac{C(\eta'/\eta)D_1\eta}{k_B}. \tag{4.1}$$

In this case, the droplet is made of hexadecane while the surrounding fluid is the bacterial suspension, opposite to the case in Chapter 2, so $\eta' = 3.47\,\text{mPa s}$ for hexadecane and $\eta = 1.00\,\text{mPa s}$ for water, and using the value found in the fitting curve $D_1 = 21.48 \pm 8.5\,\mu\text{m}^3/\text{s}$, the active temperature is $T_{\text{active}} = (2.65 \pm 1.1) \times 10^4\,\text{K}$. This value is consistent with previous works, as the study of passive tracers in a bacterial suspension [8], where the effective temperature for the tracers is 2 - 3 orders of magnitude larger than room temperature.

Another manner to estimate the active temperature is by studying the probability distribution for the droplet position. The density profile for the position of the inner hexadecane droplet is analogous to the case of the density distribution of particles in an air column under the influence of gravity, at a given temperature T. Assuming that, it reads [47, 48]

$$P(x, y, z) = A \exp(-\beta m_{\text{eff}} g z), \tag{4.2}$$

with A a normalization constant, $\beta = k_B T_{\text{active}}$ and the mass we use is the effective mass of

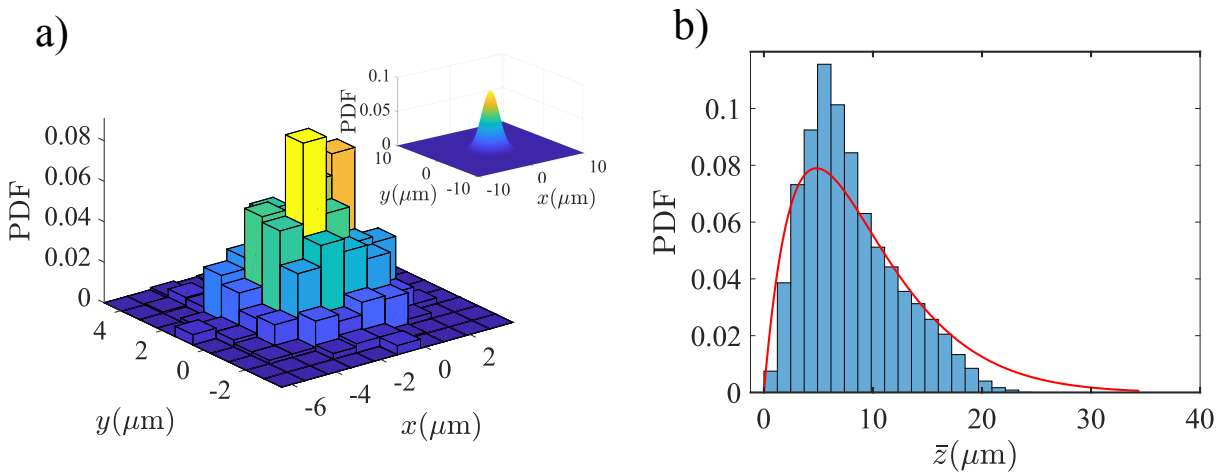

Figure 4.11: a) Probability density function for the position of the inner hexadecane droplet in the $x-y$ plane. Inset: Computed probability density function using the same parameters for the double emulsion (hexadecane droplet of $R_{\text{in}} = 34\,\mu\text{m}$ and bacterial droplet of $R_{\text{out}} = 240\,\mu\text{m}$) and a testing active temperature of $T_{\text{active}} = 2.4 \times 10^5\,\text{K}$. b) Probability density function for the position of the inner hexadecane droplet in the z axis. Red line: Computed probability density function using the same parameters for the double emulsion (hexadecane droplet of $R_{\text{in}} = 4\,\mu\text{m}$ and bacterial droplet of $R_{\text{out}} = 25\,\mu\text{m}$) the tested active temperature of the curve is $T_{\text{active}} = 2.4 \times 10^5\,\text{K}$.

the inner hexadecane droplet $m_{\text{eff}} = 4\pi R_{\text{in}}^3(\rho - \rho')/3$, with ρ and ρ' the density of the water and the hexadecane correspondingly. The probability density function (PDF) in the $x-y$ plane is obtained integrating, so $P(x,y) = \int_{z_0}^{\infty} P(x,y,z)\mathrm{d}z$ yields

$$P(x,y) = \frac{(\beta m_{\text{eff}} g)^2}{2\pi(1+\exp(\beta m_{\text{eff}} g R)[\beta m_{\text{eff}} g R - 1])} \exp(\beta m_{\text{eff}} g \sqrt{R^2 - (x^2+y^2)}) \tag{4.3}$$

where $z_0 = -\sqrt{R^2 - (x^2+y^2)}$, with $R = R_{\text{out}} - R_{\text{in}}$, taking into account that the hexadecane droplet movement is bounded by the interface of the bacterial droplet. In the case of low fluctuations, the Eq (4.3) can be approximated to a Gaussian distribution

$$P(x,y) = \frac{\beta m_{\text{eff}} g}{2\pi R} \exp\left(-\beta m_{\text{eff}} g \frac{x^2+y^2}{2R}\right). \tag{4.4}$$

Using the values of our experiments, the only variable left is the active temperature, which can be founded fitting the PDF to the data. An example of a distribution in the horizontal plane during 1 min is shown in Figure 4.11a). Using Eq.(4.4), it can be seen how should be the distribution at long times testing an active temperature of $T_{\text{active}} = 2.4 \times 10^5\,\text{K}$ and using the same parameters for this double emulsion (Fig. 4.11a) Inset). The MSD curve (Fig. 4.9) shows no saturation for all the treated videos when their duration is 1 min. Hence, it is deduced that more recording time is needed to observe a *plateau* in the MSD curve, and that will depend on the bacterial activity as well, which decreases in time. For example, using the curve in Figure 4.10a), the diffusion coefficient for an inner hexadecane droplet of $R_{\text{in}} \sim 20\,\mu\text{m}$ is $D \sim 1\,\mu\text{m}^2/\text{s}$, if $R_{\text{out}} \sim 40\,\mu\text{m}$, the estimated recording time to allow the

inner hexadecane droplet explore all the available space is $t_{rec} = \pi R^2/D \sim 20\,\text{min}$, while in the case of the same inner droplet, but if $R_{\text{out}} \sim 100\,\mu\text{m}$ the recording time to explore the available space is $t_{rec} \sim 3\,\text{h}$. As the bacterial suspension is very active just within the first 30 min, in the latter case it may not be possible to explore the whole available surface. This is like the drop in Figure 4.11a) where $t_{rec} \sim 58\,\text{h}$.

The same analysis can be done in the vertical plane. In this case, we have to integrate $P(x,y) = \int_{x^2+y^2 \leq R^2-z^2} P(x,y,z)\mathrm{d}x\mathrm{d}y$, and then changing the variable to $\bar{z}$, yields

$$P(\bar{z}) = \frac{(\beta m_{\text{eff}} g)^3 R\bar{z}(1-\bar{z}/2R)}{2[\beta m_{\text{eff}} gR\cosh(\beta m_{\text{eff}} gR) - \sinh(\beta m_{\text{eff}} gR)]} \exp(\beta m_{\text{eff}} g(R-\bar{z})) \tag{4.5}$$

An example of a distribution in the vertical plane during $\sim 12\,\text{min}$ is shown in Figure 4.11 b). Using Eq(4.5) allow us to observe the shape of the distribution at long times testing an active temperature of $T_{\text{active}} = 2.4 \times 10^5\text{K}$. It can be seen that even though it does not fit exactly, the curve has the good order of magnitude. We do not have enough data for fitting the PDF in the horizontal and vertical planes, but the measured value for the active temperature $T_{\text{active}} = 2.65 \times 10^4\,\text{K}$, and the tested values for the PDF in both planes $T_{\text{active}} = 2.4 \times 10^5\,\text{K}$, allow us to have in idea of the order of magnitude, consistent with previous works, and confirm us that both methods described above are useful in order to measure the effective or active temperature.

Chapter 5

Conclusion and perspectives

In this thesis we have performed three experiments where dense suspensions of motile bacteria are encapsulated inside emulsion drops. Moreover, we have shown that the encapsulation of these active particles can create another active particle, a motor made of motors [30]. The power extracted from this biological micromotor is quite low; for a drop of typical radius $R \sim 50\,\mu\text{m}$ we estimate it at $P_{\text{drop}} = C(\eta'/\eta)\eta R V^2 \sim 0.01\,\text{fW}$, comparable to previous works [49], but three orders of magnitude below the maximum power available from the bacterial bath for the corresponding drop volume of $5 \times 10^{-7}\,\text{mL}$ ($\sim 50\,\text{fW}$). Of course, this leaves ample room for improvement, however, most of the bacterial power will be dissipated as viscous heating, limiting the efficiency of mesoscopic bacterial motors. Also, some limitations remain a challenge due to the biological properties of the living particles, for example, the loss of activity over time. Its inhibition through an appropriate regenerating system for the chemical environment should enhance the droplets lifetime, as proven in Refs. [30, 29].

In the following we present the conclusions for each experiment.

In the first experiment we have shown that dense suspensions of motile *E.coli* encapsulated inside emulsion drops are able to transfer movement to the drops. These bacterially propelled drops perform a persistent Brownian motion, which we have systematically studied as a function of the bacterial concentration and drop radius. The diffusion coefficient, average speed and persistence time of the droplets present a wide variability. A possible origin of this variability is that, although the prepared suspensions have well controlled bacterial concentrations, the droplet production by agitation could induce concentration inhomogeneities, resulting in droplets of unequal concentration. Further studies are needed to test this hypothesis. We have shown that bacterial coordinated activity and the presence of a substrate are essential for the propulsion of the droplets. We demonstrate that bacteria drive the droplet by comparing the velocity of the center of mass of the drop with a relevant average velocity of the bacterial suspension in the bottom of the drop, and also comparing the lifetime of the bacterial collective motions with the persistence time of the droplet motion in the ballistic regime.

A remaining challenge to improve in the future, is the bacterial activity duration. In this case, the use of mutant strains with higher resistance to oxygen depletion and/or accumu-

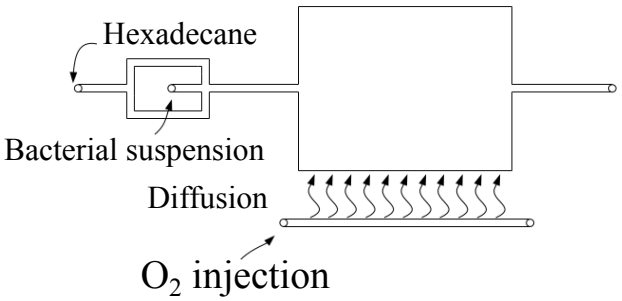

Figure 5.1: Example of microfluidic channel.

lation of detritus [38] should prove beneficial. Moreover, chemotactic behavior of bacteria represents an interesting possibility to control the drop trajectory by external, manipulable fields. Thus, bacteria could be used to transport components within the droplet, or even to transport themselves and produce, in the right place, other components of interest, like proteins or enzymes to be used in medical treatments or biochemical processes. Also, control over the droplet size is still remaining. In this sense, future experiments in polydimethylsiloxane (PDMS) microchannels can be carried out. PDMS is permeable to oxygen (diffusion coefficient of oxygen in PDMS $(9.75 \pm 1.24) \times 10^{-10}\,\mathrm{m}^2/\mathrm{s}$. [50]) and an example of microchannel design is shown in Figure 5.1, where the control of the bacterial droplets by chemotaxis can be tested. Besides, this system allows the control of the droplet radius.

In the second experiment we have shown that dense suspensions of motile magnetotactic bacteria encapsulated inside emulsion drops self-assembly into a rotary motor actuated by a controlled, external aligning magnetic field. To obtain such a complex organization, a first key-point is the ability for magnetotactic bacteria to accumulate in some areas (here being close to the droplet poles) under a uniform magnetic field. This accumulation of active swimmers, obviously limited by crowding, results in an instability triggering a coordinated motion at the scale of the droplet. The second crucial point relies on the original properties of this “active magnetic fluid". Any swimming kinematics inducing a change in the magnetic moment orientation of the bacteria with respect to the applied magnetic field, is bound to produce torque on the surrounding fluid. Interestingly, this situation is reversed compared with the standard synchronous motor, exemplified by the magnetic stirrer of chemical labs, which follows the rotation of a rotating magnetic field. In our case, a swimming bacterium carrying a magnetic moment is rotated and creates a torque due to the confinement in a droplet, while the magnetic field direction remains fixed.

We have seen that the misalignment of magnetotactic bacteria respect the external field was key in order to exert the torque on the surrounding fluid, and we expect a similar behavior for other types of autonomous swimmers, confined and orientable by any external field (electric field, light,...), maybe opening a new branch of theoretical and experimental investigations. It would probably be fruitful to exploit it by an adapted design of a microfluidic environment. PDMS microchannels can be made, having several circular wells, to create several rotating biological micromotors. To test future ways to recover the energy from the bacterial micromotor, a helix can be fixed in the center of the well, in order to rotate with the spinning of the bacterial suspension (Fig.5.2a). Another future experiment, can be the

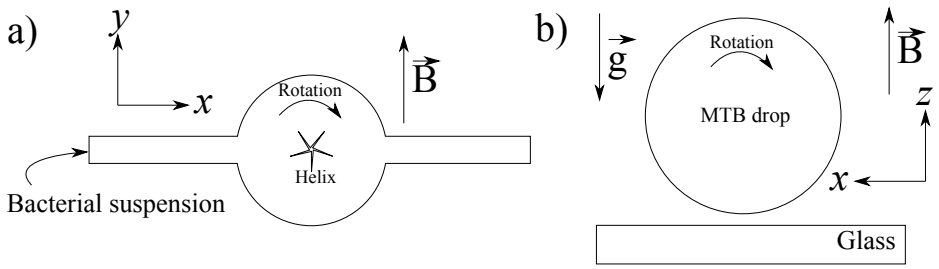

Figure 5.2: Future experiments on MTB suspension. a) Microfluidic channel with a helix at the center of a circular well. When the magnetic field is set, the bacterial suspension should start rotating, moving the helix as well. b) Testing the MTB drop in a vertical magnetic field. In the case the vortex is formed spinning parallel to the substrate, the drop could propel and with the magnetic field it could be possible to control the direction and speed of the drop movement.

displacement of the drop of magnetotactic bacteria. So far, we performed experiments where the magnetic field laid on the horizontal plane. Could be interesting to test a magnetic field on the vertical plane and see if the vortex is formed parallel to the horizontal plane which would enhance the drop displacement as in the *E. coli* experiment (Fig.5.2b). Here, we could control the speed and the propelling direction as well.

In the third experiment, we have shown that dense suspensions of motile *E. coli* encapsulated inside double emulsion drops create internal flows perturbing the inner oil droplet position. We have measured the fluctuating position of this inner oil droplet, which is trapped on the top of the bacterial droplet due to buoyancy, because hexadecane is less dense than water. We have shown that in the horizontal plane the inner oil droplet performs a persistent random walk with a persistence time $\tau \sim 0.3\,\mathrm{s}$ consistent with the lifetime of the bacterial collective motions in Chapter 1. The diffusion coefficient in the horizontal plane depends inversely on the inner droplet radius, and we compare it with the thermal diffusion coefficient. It allow us to compute an effective or active temperature, which has a value of $2.7 \times 10^4\mathrm{K}$, two orders of magnitude larger than room temperature and consistent with previous works. The vertical plane was also studied, revealing that the diffusion coefficient in the vertical axis is less than in the horizontal axis, what was expected due to buoyancy. The probability density function (PDF) for the droplet position is studied. These expressions for the PDF stand for long time position distributions and they give us another way to compute the active temperature. In the horizontal plane, even though the recording time was 1 min, we tested an active temperature of $2.4 \times 10^5\mathrm{K}$. In the vertical plane we did the same, testing the same value for the temperature. This value, in the horizontal and vertical plane is one order of magnitude larger than the first value we measured from the diffusion coefficient, but it is still in the good order of magnitude. Despite the lack of data, these preliminary experiments were useful to learn how to stabilize the double emulsion and to define protocols as well, opening the possibility of using a new system to study fluctuations due to bacterial swimming.

Evidently, more experiments are needed. It is important that they be performed systematically for different radii and bacterial concentration in order to have a good measurement of the active temperature. In terms of recording time, it will be necessary that independently of the size of the droplets, their radii difference $R = R_{\mathrm{out}} - R_{\mathrm{in}}$, be not larger than $\sim 20 - 30\,\mu\mathrm{m}$,

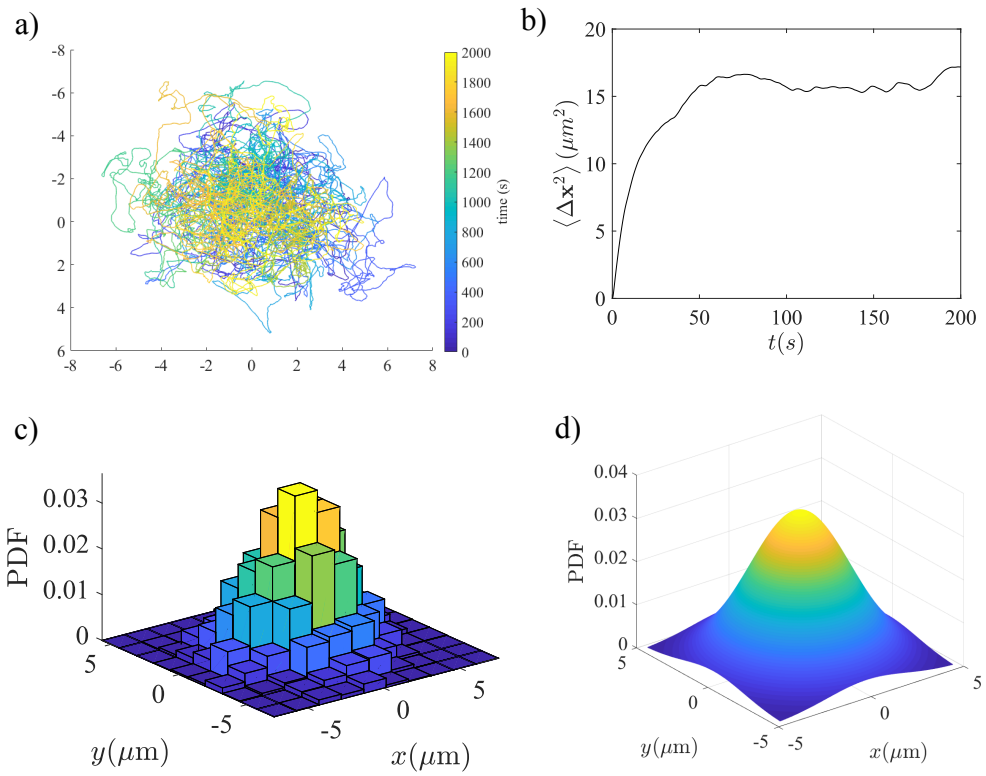

Figure 5.3: New results on bacterial double emulsion performed by Cristian Villalobos. The shell parameters are $R_{\text{out}} = 22\,\mu\text{m}$ and $R_{\text{in}} = 8\,\mu\text{m}$. a) Trajectory of the inner hexadecane droplet during 33 min recorded at 10 fps. b) Mean square displacement for the complete trajectory. Is is observed clearly the saturation due to the confinement. c) Distribution of the position of the droplet during the whole video. d) Fitting of the distribution, using Eq(4.3). The fitted active temperature is $(1.3 \pm 8.9) \times 10^5\,\text{K}$. The R-squared of the fitting is 0.86.

to have enough time to explore the available space within the good bacterial activity time ($\leq$30 min), and therefore perform films with $t_{\text{rec}} = 30\,\text{min}$. As we will study the persistence time, but also the diffusion coefficient at long times, a first film, recorded at $30 - 50$ fps for 1 min would be fine to recover the ballistic part in the MSD curve, while a second film at 10 fps for 30 min is good to study the diffusion of the inner hexadecane droplet. Example of an experiment carried out by Cristian Villalobos in these conditions is shown in Figure 5.3. This is a shell of radii $R_{\text{out}} = 22\,\mu\text{m}$ and $R_{\text{in}} = 8\,\mu\text{m}$ recorded at 10 fps for 33 min. The complete trajectory (Fig.5.3a) along with the MSD show a saturation (Fig.5.3b), meaning that in this case, the inner droplet could explore the complete available space. The active temperature can be computed from the position distribution (Fig.5.3c) using Eq(4.3). Fitting the PDF using this function gives an active temperature of $(1.3 \pm 8.9) \times 10^5\,\text{K}$ (Fig.5.3d). Finally, experiments for the z coordinate should be performed systematically as well, changing the same parameters (e.g. drop size and bacterial concentration), and respecting the same recording times and fps, but these experiments should be carried out at the Gulliver lab at the ESPCI in France, in order to use the rotating confocal microscope.

Bibliography

[1] M. C. Marchetti, J.-F. Joanny, S. Ramaswamy, T. B. Liverpool, J. Prost, M. Rao, and R. A. Simha. Hydrodynamics of soft active matter. *Rev. Mod. Phys.*, 85:1143–1189, 2013.

[2] R. Sknepnek and S. Henkes. Active swarms on a sphere. *Phys. Rev. E*, 91(2):022306, 2015.

[3] G. Popkin. The physics of life. *Nature*, 529(7584):16–18, 2016.

[4] A. Baskaran and M.C. Marchetti. Statistical mechanics and hydrodynamics of bacterial suspensions. *PNAS*, 106(37):15567–15572, 2009.

[5] E. Altshuler, G. Miño, C. Pérez-Penichet, L. del Río, A. Lindner, A. Rousselet, and E. Clément. Flow-controlled densification and anomalous dispersion of e. coli through a constriction. *Soft Matter*, 9:1864–1870, 2013.

[6] J. Hill, O. Kalkanci, J. L. McMurry, and H. Koser. Hydrodynamic surface interactions enable *Escherichia coli* to seek efficient routes to swim upstream. *Phys. Rev. Lett.*, 98(6):068101, 2007.

[7] R. Rusconi, J.S. Guasto, and R. Stocker. Bacterial transport suppressed by fluid shear. *Nature physics*, 10(3):212–217, 2014.

[8] Xiao-Lun Wu and Albert Libchaber. Particle diffusion in a quasi-two-dimensional bacterial bath. *Phys. Rev. Lett.*, 84:3017–3020, 2000.

[9] H. M. López, J. Gachelin, C. Douarche, H. Auradou, and E. Clément. Turning bacteria suspensions into superfluids. *Phys. Rev. Lett.*, 115:028301, 2015.

[10] J Gachelin, A Rousselet, A Lindner, and E Clément. Collective motion in an active suspension ofEscherichia colibacteria. *New J. Phys.*, 16:025003, 2014.

[11] K. Drescher, J. Dunkel, L. H. Cisneros, S. Ganguly, and R. E. Goldstein. Fluid dynamics and noise in bacterial cell-cell and cell-surface scattering. *Proc. Natl. Acad. Sci. USA*, 108:10940–10945, 2011.

[12] Mihails Belovs, Rudolfs Livanovics, and Andrejs Cebers. Hydrodynamic synchronization of pairs of puller type magnetotactic bacteria in a high frequency rotating magnetic field.

Soft Matter, 15(7):1627–1632, 2019.

[13] H.C. Berg. *E. coli in motion*. Springer, New York, 2004.

[14] Dorothée Murat, Marion Hérisse, Leon Espinosa, Alicia Bossa, François Alberto, and Long-Fei Wu. Opposite and coordinated rotation of amphitrichous flagella governs oriented swimming and reversals in a magnetotactic spirillum. *Journal of Bacteriology*, 197(20):3275–3282, 2015.

[15] R Blakemore. Magnetotactic bacteria. *Science*, 190(4212):377–379, 1975.

[16] René Uebe and Dirk Schüler. Magnetosome biogenesis in magnetotactic bacteria. *Nature Reviews Microbiology*, 14:621 EP, 2016.

[17] D. Schüler and R. B. Frankel. Bacterial magnetosomes: microbiology, biomineralization and biotechnological applications. *Applied Microbiology and Biotechnology*, 52(4):464–473, 1999.

[18] Ouajdi Felfoul, Mahmood Mohammadi, Samira Taherkhani, Dominic de Lanauze, Yong Zhong Xu, Dumitru Loghin, Sherief Essa, Sylwia Jancik, Daniel Houle, Michel Lafleur, Louis Gaboury, Maryam Tabrizian, Neila Kaou, Michael Atkin, T. é Vuong, Gerald Batist, Nicole Beauchemin, Danuta Radzioch, and Sylvain Martel. Magneto-aerotactic bacteria deliver drug-containing nanoliposomes to tumour hypoxic regions. *Nature Nanotechnology*, 11:941 EP, 2016.

[19] I. D. Vladescu, E. J. Marsden, J. Schwarz-Linek, V. A. Martinez, J. Arlt, A. N. Morozov, D. Marenduzzo, M. E. Cates, and W. C. K. Poon. Filling an emulsion drop with motile bacteria. *Phys. Rev. Lett.*, 113:268101, 2014.

[20] A. Cheng Hou Tsang and E. Kanso. Circularly confined microswimmers exhibit multiple global patterns. *Phys. Rev. E*, 91(4):043008, 2015.

[21] Jocelyn Dunstan, Gastón Mino, Eric Clement, and Rodrigo Soto. A two-sphere model for bacteria swimming near solid surfaces. *Phys. Fluids*, 24(1):011901, 2012.

[22] O. Sipos, K. Nagy, R. Di Leonardo, and P. Galajda. Hydrodynamic trapping of swimming bacteria by convex walls. *Phys. Rev. Lett.*, 114(25):258104, 2015.

[23] A. Wysocki, J. Elgeti, and G. Gompper. Giant adsorption of microswimmers: Duality of shape asymmetry and wall curvature. *Phys. Rev. E*, 91(5):050302, 2015.

[24] P. Galajda, J. Keymer, P. Chaikin, and R. Austin. A wall of funnels concentrates swimming bacteria. *Journal of Bacteriology*, 189(23):8704–8707, 2007.

[25] A. Guidobaldi, Y. Jeyaram, I. Berdakin, V. V. Moshchalkov, C. A. Condat, V. I. Marconi, L. Giojalas, and A. V. Silhanek. Geometrical guidance and trapping transition of human sperm cells. *Phys. Rev. E*, 89(3):032720, 2014.

[26] K. M. Jones, H. Kobayashi, B.W. Davies, M.E. Taga, and G.C. Walker. How rhizo-

bial symbionts invade plants: the sinorhizobium-medicago model. *Nat. Rev. Microbiol.*, 5(8):619–633, 2007.

[27] J.M. Collinson, L. Morris, A.I. Reid, T. Ramaesh, M.A. Keighren, J.H. Flockhart, R.E. Hill, S.S. Tan, K. Ramaesh, B. Dhillon, and J.D. West. Clonal analysis of patterns of growth, stem cell activity, and cell movement during the development and maintenance of the murine corneal epithelium. *Developmental Dynamics*, 224(4):432–440, 2002.

[28] Hugo Wioland, Francis G. Woodhouse, Jörn Dunkel, John O. Kessler, and Raymond E. Goldstein. Confinement stabilizes a bacterial suspension into a spiral vortex. *Phys. Rev. Lett.*, 110:268102, 2013.

[29] Felix C. Keber, Etienne Loiseau, Tim Sanchez, Stephen J. DeCamp, Luca Giomi, Mark J. Bowick, M. Cristina Marchetti, Zvonimir Dogic, and Andreas R. Bausch. Topology and dynamics of active nematic vesicles. *Science*, 345:1135–1139, 2014.

[30] Tim Sanchez, Daniel T. N. Chen, Stephen J. DeCamp, Michael Heymann, and Zvonimir Dogic. Spontaneous motion in hierarchically assembled active matter. *Nature*, 491:431–434, 2012.

[31] E. Lauga, W. R. DiLuzio, G. M. Whitesides, and H. A. Stone. Swimming in circles: Motion of bacteria near solid boundaries. *Biophys. J.*, 90:400–412, 2006.

[32] R. Di Leonardo, D. Dell'Arciprete, L. Angelani, and V. Iebba. Swimming with an image. *Phys. Rev. Lett.*, 106:038101, 2011.

[33] Allison P. Berke, Linda Turner, Howard C. Berg, and Eric Lauga. Hydrodynamic attraction of swimming microorganisms by surfaces. *Phys. Rev. Lett.*, 101:038102, 2008.

[34] Gabriel Ramos, Maria Luisa Cordero, and Rodrigo Soto. Bacteria driving droplets. *arXiv:1912.04195 [cond-mat.soft]*, 2019.

[35] H. H. Wensink, J. Dunkel, S. Heidenreich, K. Drescher, R. E. Goldstein, H. Löwen, and J. M. Yeomans. Meso-scale turbulence in living fluids. *Proc. Natl. Acad. Sci. USA*, 109:14308–14313, 2012.

[36] E. Lauga and T. R Powers. The hydrodynamics of swimming microorganisms. *Rep. Prog. Phys.*, 72:096601, 2009.

[37] Benoit Vincenti, Gabriel Ramos, Maria Luisa Cordero, Carine Douarche, Rodrigo Soto, and Eric Clement. Magnetotactic bacteria in a droplet self-assemble into a rotary motor. *Nature Communications*, 10(1):5082, 2019.

[38] Juan E. Keymer, Peter Galajda, Guillaume Lambert, David Liao, and Robert H. Austin. Computation of mutual fitness by competing bacteria. *Proc. Natl. Acad. Sci. USA*, 105:20269–20273, 2008.

[39] Tohru Minamino, Yasuo Imae, Fumio Oosawa, Yuji Kobayashi, and Kenji Oosawa. Effect of intracellular ph on rotational speed of bacterial flagellar motors. *J. Bacteriol.*,

185:1190–1194, 2003.

[40] F. P. Bretherton. The motion of long bubbles in tubes. *J. Fluid Mech.*, 10:166–188, 1961.

[41] W. Thielicke and E.J. Stamhuis. Pivlab - towards user-friendly, affordable and accurate digital particle image velocimetry in matlab. *J. Open Res. Softw.*, 2:e30, 2014.

[42] K. Martens, L. Angelani, R. Di Leonardo, and L. Bocquet. Probability distributions for the run-and-tumble bacterial dynamics: An analogy to the lorentz model. *The European Physical Journal E*, 35(9):84, 2012.

[43] Andrey Sokolov and Igor S. Aranson. Physical properties of collective motion in suspensions of bacteria. *Phys. Rev. Lett.*, 109:248109, 2012.

[44] W. N. Bond. Lxxxii. bubbles and drops and stokes' law. *The London, Edinburgh, and Dublin Philosophical Magazine and Journal of Science*, 4:889–898, 1927.

[45] Felix Popp, Judith P. Armitage, and Dirk Schüler. Polarity of bacterial magnetotaxis is controlled by aerotaxis through a common sensory pathway. *Nature Communications*, 5(1):5398, 2014.

[46] Jiadong Fan, Zhibin Sun, Jian Zhang, Qingjie Huang, Shengkun Yao, Yunbing Zong, Yoshiki Kohmura, Tetsuya Ishikawa, Hong Liu, and Huaidong Jiang. Quantitative imaging of single unstained magnetotactic bacteria by coherent x-ray diffraction microscopy. *Analytical Chemistry*, 87(12):5849–5853, 2015.

[47] Walter Greiner, Ludwig Neise, and Stöcker. *Thermodynamics and Statistical Mechanics*. Springer-Verlag New York, 1 edition, 1995.

[48] Felix Ginot, Alexandre Solon, Yariv Kafri, Christophe Ybert, Julien Tailleur, and Cecile Cottin-Bizonne. Sedimentation of self-propelled janus colloids: polarization and pressure. *New Journal of Physics*, 20(11):115001, nov 2018.

[49] R. Di Leonardo, L. Angelani, D. Dell'Arciprete, G. Ruocco, V. Iebba, S. Schippa, M. P. Conte, F. Mecarini, F. De Angelis, and E. di Fabrizio. Bacterial ratchet motors. *Proc. Natl. Acad. Sci. USA*, 107:9541–9545, 2010.

[50] Sanchari Chowdhury, Venkat R. Bhethanabotla, and Rajan Sen. Measurement of oxygen diffusivity and permeability in polymers using fluorescence microscopy. *Microscopy and Microanalysis*, 16(6):725–734, 2010.

Appendix A

Protocols

A.1 LB preparation

This is a rich medium to grow bacteria such as *E. coli*. Generally it comes already prepared in powder and it is necessary to add distilled water in the ratio indicated in the package. If not, the medium is prepared with these reagents:

- 10 g tryptone
- 5 g yeast extract
- 5 g NaCl
- Add distilled water to have 1 L

Then, agitate to mix, and autoclave. It is important to say that it must be autoclaved the same day it is prepared. After autoclaving, let the bottle cool and then place it inside a 4 °C fridge.

A.2 Agar plates

Before filling the petri dishes, it is necessary to prepare the LB agar. For making 4 agar plates of a size 100 mm x 15 mm, mix in a 250 mL bottle:

- 100 mL of LB
- 1.5 g of Agar

Then autoclave, and let the bottle cool. It can be stored at ambient temperature. To prepare the agar plates, follow these steps:

1) Heat the bottle in a microwave until it boils and everything is liquid. Take the bottle with gloves to avoid burning.
2) When the bottle is cold enough to touch it by hand, but the solution is still liquid, pour it inside 50 mL Falcon tubes.
3) Place the petri dish under the hood, and then pour gently 25 mL of the liquid LB agar inside the petri dish. Try to do it at once, to prevent bubble formation.
4) Let the agar plates cool until it solidifies. Then, cover the plates, seal with Parafilm and store them upside down in a 4 °C fridge.

A.3 *E. coli* stock

This protocol is for the W3110 strain. For other strains, the same steps can be applied but the parameters on the incubator may change (temperature and agitation).

The main stock of *E. coli* is preserved in a −80 °C fridge. It is important to check the amount of tubes to decide if is necessary to prepare a new stock. Cryotubes are recommended, but Eppendorf tubes of 2 mL can be used as well. In the following we give the steps to prepare a new stock:

1) Inoculate an agar plate using bacteria from a −80 °C stock. If it is not possible, it can be done from a −20 °C stock. This is performed using an inoculating loop of 1 µL as it is shown in Figure A.1. In case of using plastic sterile inoculation loops, start from Figure A.1b).

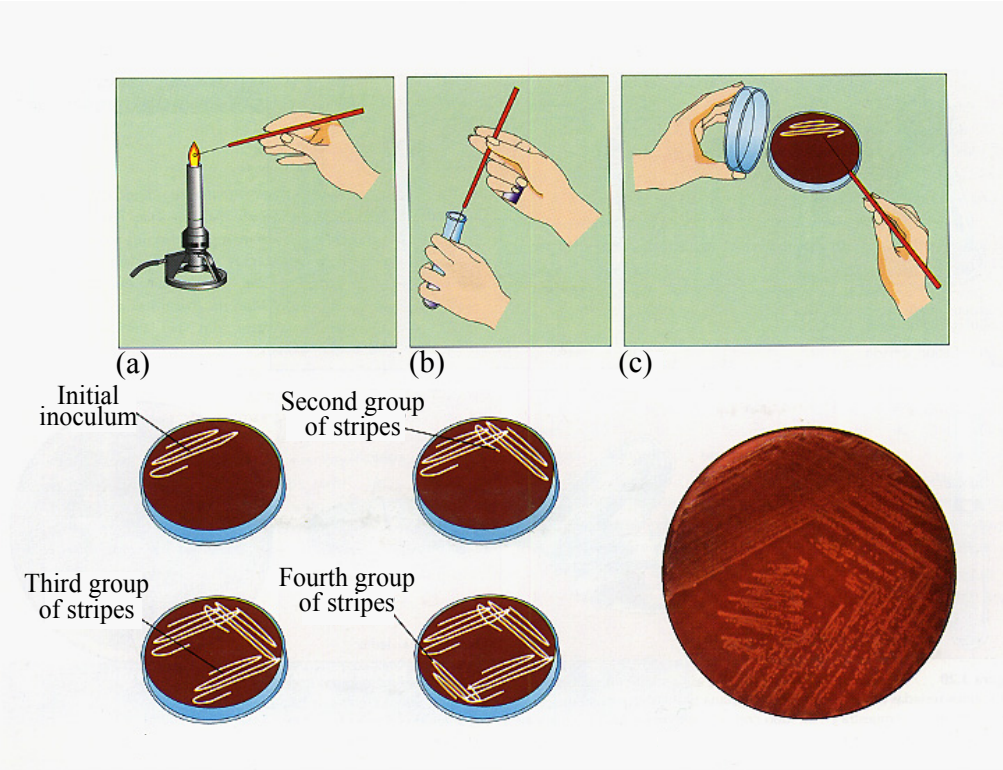

Figure A.1: Example showing how to inoculate an agar plate. Extracted from microbiologiauasd.blogspot.com

2) The agar plates are incubated at 28 °C between 1 and 2 days, until colonies appear (Fig. A.2).
3) Pick up one single isolated colony (Fig. A.2 green circle), either with an inoculating loop or with a micropipette tip, and place it inside a Falcon tube with 10 mL of fresh LB medium. Place the tube inside the incubator at 28 °C and 180 rpm and wait 1 day to make an overnight. It is important to say that the cap of the tube must be a bit loose, preventing things to enter and contaminate the culture, but allowing the transfer

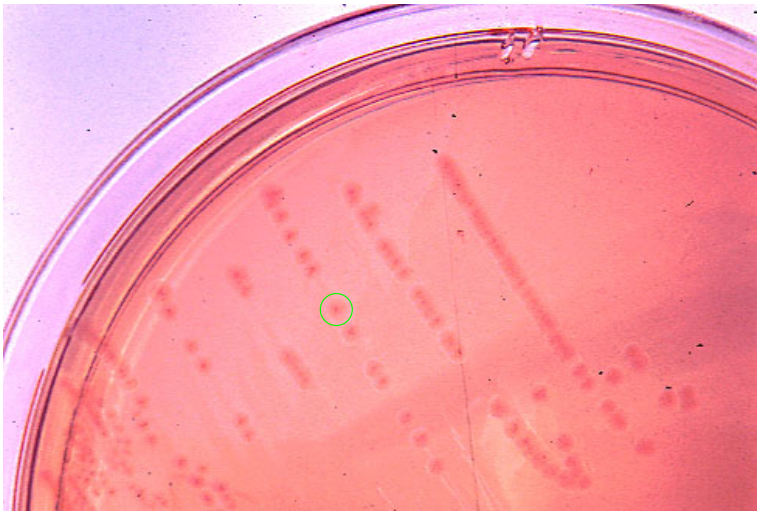

Figure A.2: Example of colonies in agar plate. Lines are merged colonies, while *dots* are isolated colonies, like the one within the green circle. Modified from www.medschool.lsuhsc.edu

of oxygen with the environment. Also, the tube must be placed inclined, increasing the liquid surface in contact with the air.

4) The next day, check the overnight culture in the microscope. If the bacterial motility is fine, prepare a culture inoculating part of the overnight in fresh LB in a ratio 1:1000 (eg. Take 10 µL from the overnight in 10 mL of fresh LB medium) then place the tube in the incubator (28 °C and 180 rpm).
5) Check the growth of the culture. In the exponential phase, between OD $\sim$ 0.2 and OD $\sim$ 0.3, take out the tubes from the incubator.
6) Mix 500 µL of bacterial culture with 1000 µL of Glycerol 30% v/v inside a cryotube. Seal the tube and agitate manually. To prepare 1000 µL of Glycerol 30%, use 300 µL of Glycerol 99% mixed with 700 µL of fresh LB.
7) Freeze the cryotube in a -20 °C for 1 day. Then, transfer the cryotube to a -80 °C fridge. If liquid nitrogen is available, just drop the cryotube inside for some seconds, take it out and then place it directly inside the -80 °C fridge. Repeat this for every cryotube stock.

A.4 FSM preparation

The Flask Standard Medium (FSM) is the culture medium for magnetotactic bacteria. Mix the next reagents in a 1 L bottle:

- 10 mL of Hepes buffer (1 M)
- 3.8 mL of Potassium lactate (50%)
- 3 g Soy peptone
- 0.1 g Yeast extract
- 1 mL of KH_2PO_4
- 4 mL of $NaNO_3$ (1 M)
- 6 mL of $MgSO_4$ $7H_2O$ (0.1 M)
- 5 mL of Ferric citrate (10 mM)

After mixing the reagents, add 970 mL of distilled water. Agitate until everything is dissolved. Then, sterilize the medium using a Nalgene Filter.

The Hepes buffer and the Potassium lactate are already liquid. To prepare the other solutions:

1) In a Falcon tube, dissolve 1 g of KH_2PO_4 in 10 mL of distilled water.
2) In a Falcon tube, dissolve 1 g of $NaNO_3$ in 10 mL of distilled water.
3) In Falcon tube, put 10 mL of distilled water and add 0.246 g of $MgSO_4$ $7H_2O$.
4) In a beaker, dissolve 0.250 g of Ferric citrate in 100 mL of distilled water. Use a magnetic stirrer during 15 min while heating. At the beginning it is cloudy and the final solution must be transparent, with a yellowish color.

Use of the Nalgene filter.

1) Pour the medium in the cylindrical container of the filter, then close this container by putting the cap.
2) Connect the Nalgene filter to a vacuum pump. Actuate the pump, and the medium should be drawn to the bottle connected to the filter.
3) Close the new bottle and store in a 4 °C fridge.

In case that not all the medium prepared in the 1 L bottle is used, or in case that there is no Nalgene filter, it can be autoclaved and stored in the 4 °C fridge.

A.5 MTB culture

To prepare a new culture of magnetotactic bacteria follow these steps:

1) Take the bottle with FSM from the 4 °C fridge.
2) Put 10 mL of FMS inside each Hungate tube.
3) Bubble each tube with N_2 as indicated in Fig. A.3. and then close each tube firmly with the plastic cap.
4) Autoclave the Hungate tubes
5) When the Hungate tubes are cold (e.g. room temperature) take a stock cryotube from the −80 °C fridge.
6) When the stock is completely melted, fill a 5 mL syringe using all the content from the cryotube. Incline the Hungate tube, pierce the rubber cap with the syringe (while the plastic cap is still on), and drop little droplets of bacterial suspension until 300 µL are inoculated (Fig.A.4). Repeat for each Hungate tube.
7) Place the Hungate tubes inside the incubator at 28 °C and 180 rpm.
8) Let bacteria grow between 3 to 5 days until they have an OD∼0.14.

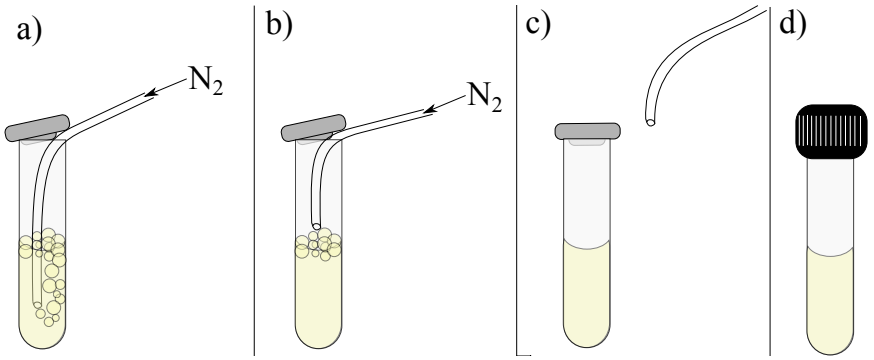

Figure A.3: Bubbling N_2 inside Hungate tubes. a) Start bubbling at the bottom of the tube, while keeping the rubber cap almost closing the tube. b) Take out the tubing, keeping the rubber cap in the same position. c) At the instant the tubing is out the tube, close completely with the rubber cap. This must be done quickly. d) Close the tube firmly with the plastic cap.

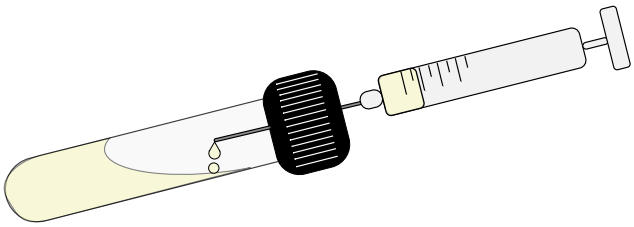

Figure A.4: MTB incoulation from a −80 °C stock. It is important to incline the tube for inoculation, paying attention of dropping the bacterial suspension on the FSM medium and not directly on the glass.

A.6 MTB stock

To make a stock of magnetotactic bacteria:

1) Prepare a culture as indicated in the protocol for the MTB culture (Appendix A.5).
2) Check the motility of bacteria in the microscope.
3) If bacteria swim normally (good motility), mix 1000 µL of bacterial culture with 400 µL of Glycerol 60% v/v inside a cryotube. Agitate manually and place the cryotube inside liquid nitrogen.
4) Take the cryotube out from the liquid nitrogen and then place it directly inside the −80 °C fridge. Repeat this for every cryotube stock.

For preparing 1000 µL of Glycerol 60%, mix 600 µL of Glycerol 99% with 400 µL of FSM.

A.7 MMA preparation

The minimal medium A is a phosphate buffer that allows bacteria to live, but prevents cell division. First of all, two buffer solution must be prepared, each one in a 500 mL bottle:

- Dissolve 48 g of NaH_2PO_4 in 400 mL of distilled water (1 M)
- Dissolve 70 g K_2HPO_4 in 400 mL of distilled water (1 M)

Autoclave both bottles and store in a 4 °C fridge.

To prepare a MMA stock x100 in a 500 mL bottle add the following reagents:

1) 1.48 g of EDTA
2) 37.2 g of Sodium lactate
3) 240 mL of K_2HPO_4 buffer solution
4) 160 mL of NaH_2PO_4 buffer solution

To use this MMA stock, dilute 100 times. For example, for a 50 mL Falcon tube, use 0.5 mL of the MMA stock and add 49.5 mL of distilled water.

A.8 Motility buffer

The motility buffer is a phosphate buffer similar to MMA, that allows bacteria to live but prevents cell division, but it is prepared in order to enhance bacterial swimming.
First, a potassium phosphate buffer is prepared. In two separate bottles add the following:

- Dissolve 8.7 g of K_2HPO_4 in 50 mL of distilled water (1 M solution).
- Dissolve 6.8 g of KH_2PO_4 in 50 mL of distilled water (1 M solution).

Now, mix 2.46 mL of K_2HPO_4 and 1.54 mL of KH_2PO_4, and add distilled water to obtain 40 mL of resulting solution (0.1 M).

For the Motility buffer (50 mL):

- 50 µL of EDTA
- 50 µL of l-methionine (1 mM)
- 500 µL of Sodium lactate (1 M)
- 5 mL of Potassium phosphate buffer (0.1 M)
- 44.4 mL of distilled water

Dissolve the reagents and filter using a 0.22 µm Nalgene filter as indicated in the FSM protocol.

A.9 M9G preparation

To prepare M9 Glucose minimal media:

1) Dissolve 5.64 g of M9 salt in 100 mL of distilled water. Autoclave and let it cool down.
2) Add 2 g of Glucose
3) Add 0.5 g of Casamino acids
4) Add 50 µL of $CaCl_2$ (1M)
5) Add 1 mL of $MgSO_4$ (1M)
6) Add water to obtain 500 mL
7) Filter using a 0.22 µm Nalgene filter as indicated in the FSM protocol (Appendix A.4).

A.10 Chamber fabrication

To fabricate the chamber in the first experiment:

1) Clean a 50.8 mm diameter and 500 µm thick circular glass wafer in a plasma cleaner for 7 min
2) Cover the circular glass wafer with SU-8 photoresist (Gersteltec GM1075) and spin coat 100 s at 500 rpm.
3) Put the spin coated wafer on a hot plate for 30 min at 40 °C (Relax time). **Important:** Be sure the hot plate is well leveled and place the wafer in the center of the hot plate if possible. If the hot plate is not completely horizontal, the SU-8 layer will not be uniform and the optical lithography machine will not accept the wafer.
4) Rise the temperature to 120 °C for 50 min (Pre-bake)
5) Put the wafer in the optical lithography machine. If it does not accept the wafer, return to 4). For better results, the time in 4) can be extended. If the machine accepts the wafer, expose it with a dose of 1000 mJ/cm^2.
6) Place the exposed wafer on the hot plate 2 h 30 min at 95 °C (Post-bake)
7) Let the exposed wafer to cool down for 1 h (delay time).
8) Develop in PGMEA between 20 to 30 min.
9) Clean the wafer with isopropanol.

The previous steps are for a thickness of 400 µm. For other thickness, adjust the steps according to the datasheet of Gersteltec GM1075.

The chamber was previously designed in AutoCad. It was just two concentric squares. The outer square had 1.5 cm side, and the inner a 1 cm side. The AutoCad design is converted in order to be recognized and used by the optical lithography machine.

A.11 Double emulsion device fabrication

In a first step we look for two capillaries that match each other, in particular, a cylindrical capillary inside the squared one (Fig.4.1). Then, the cylindrical capillary is cut using a Vertical Pipette Puller (Model 720 David Kopf). The capillary is fixed on the top and the bottom and and the machine is set on. It will melt the glass and then will push down in order to cut the capillary (Fig.A.5a and A.5b). The result is two sharp pieces. The upper one is used for the outlet section and the other one, which is narrow, will be the inlet(Fig.A.5c). Now, the tips are cut. To do so, the capillary is placed in a Micro Forge (MF830) (Fig.A.6a and A.6b), where there is a melting glass, so the tip is down to the melting glass, then the heating is stopped, everything gets solid again, and finally the capillary is pushed up very quickly in order to break the glass, to make a horizontal straight cut (Fig.A.6c and A.6d).

(a)

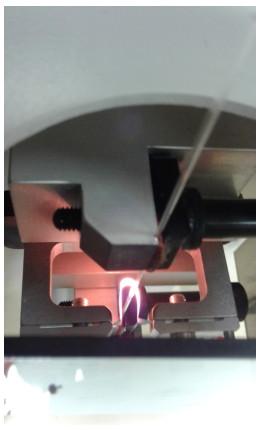

(b)

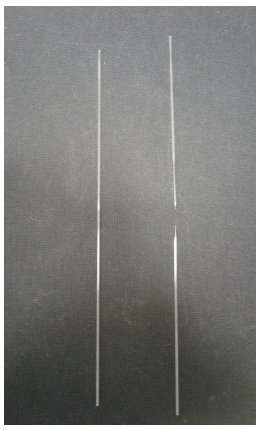

(c)

Figure A.5: (a) Vertical Pipette Puller. Two values are needed to set up. The heater and the solenoid. The values used are 9.0 for the first one and 4.0 for the second one. (b) Closer view of the cutting process. We observe the heating part which melts the glass. (c) Comparison between two capillaries before and after cutting. The upper part is always wider.

Now, the silanization process is performed. It consists of preparing a solution with chloroform and hexane in a ratio 1:4 (in our case 2 mL of chloroform and 8 mL of hexane were used) and the silane, Octadecyltrichlorosilane (OTS) (8 µL minimum). So, before putting the capillary (outlet in our case) in the solution, all the capillaries are cleaned in the ultrasonic bath, first with ethanol, then water and finally acetone. Every time about 2 or 3 min. After that, the outlet is taken and placed into the solution during 5 min, then the capillary is cleaned with chloroform, and a soft bake is done for 2 h at 120 °C. After the soft bake, the outlet is rinsed with water and then with ethanol.
In the meanwhile, the surface containing the capillaries can be prepared. Three rectangular glass slides (76×52×1 mm) are used. The third one is cut by half, and piece is used to make little pieces that will be used to glue and join the three glass slides. Everything is done with Epoxi. Also, the injection points need to be prepared. They are made of syringe needles, where the sharp point is cut, and holes are made in the plastic base of the needle in order to fit the capillaries. The typical diameter of the needles is 900 µm but also there are narrower, of 400 µm.

(a)

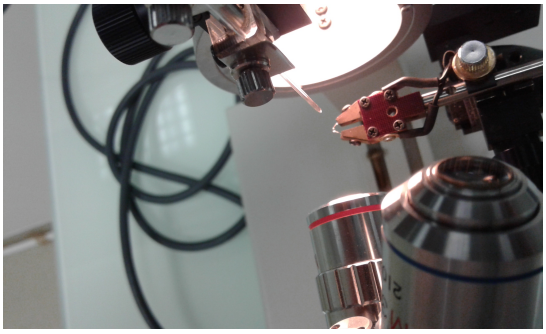

(b)

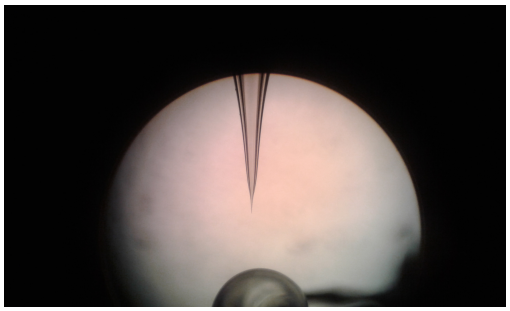

(c)

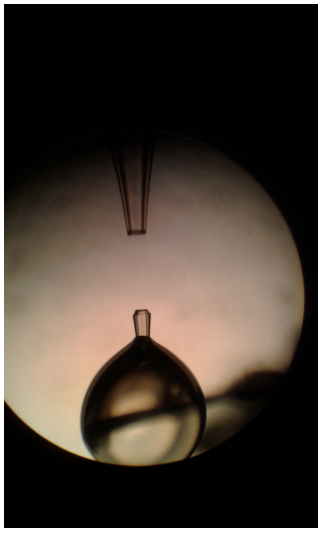

(d)

Figure A.6: (a) MicroForge. Here the capillaries tips are cut. (b) Closer view of the cutting process. We observe the capillary in the upper side, which is approaching the melted glass. All this process is observed by means of a graduated objective. Each graduate is 20 µm. (c) Tip near the melted glass. When they touch each other, they melt together and the glass comes up by capillarity, then heating is stopped when the melted glass attain the desired hight, and it is cooled down. (d) When it is cold enough, the capillary is pulled up as quick as possible, breaking the tip at the desired hight.

When everything is ready, the square capillary is glued on the glass surface. To do so, the Epoxi is prepared on weigh boat using a stick. A portion of the epoxi is poured over the capillary, like an arch, being careful that no glue is under the capillary. When is ready, the setup is placed on the microscope and we do the *alignment* process. There are three things to check. First be sure that they are parallel one in front the other. Second, we focus the image until lines are seen on the borders, and the capillaries are rotated until they look focused in the same way. Third, both the capillaries are separated approximately the same distance than the outlet diameter. Then, the round capillaries are glued to fix them (Fig.A.7a and A.7b).
Finally, the injection points are glued. To do so, just a little bit of Epoxi is putted on the bottom of plastic base of the needles, right after preparing the glue. Then, the needles are putted on the capillaries. Now, wait some seconds until the glue becomes more viscous,

then more Epoxi is poured around the needle, paying attention that it doesn't go inside the base of the needle, and a *bridge* of glue is done over the holes of the base of the needle, just where it fits the capillary. Wait until the glue gets hard, and then put more Epoxi (Just fresh, it is not necessary to wait this time), ensuring no leakage. Finally, we put tubing in the free capillary, where the final double emulsion will come out, and it is glued with Epoxi. After all this process, the device is finished (Fig.A.7c), and we test the device introducing pure water, to observe if there is either leakage or blockage. If not, it is ready to work.

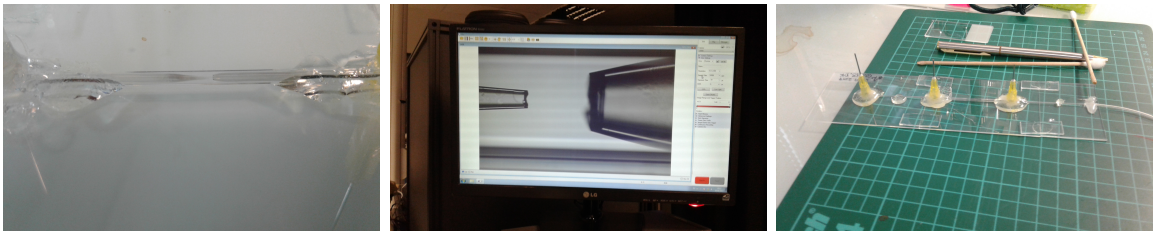

(a) (b) (c)

Figure A.7: (a) All capillaries after the alignment process. We observe each one in front of the other, and also some glue on both sides fixing the squared capillary. (b) When doing the alignment, and also when working we observe the capillaries in the microscope (10x). In this case we see they are well aligned and separated by a distance approximately equal to the outlet diameter. (c) Final device with needles connected. At this moment it is ready to work.

A.12 Differences in *E. coli* culture methods

The bacterial culture method used in Chapter 3 is different from Chapter 2 because we followed the protocol of the PMMH lab in France to grow the strain available in this lab (RP437), which is different from the strain in Chile (W3110). In terms of swimming, both strains have the same features (eg. run and tumble), but the difference is in the way they express the fluorescence. While the W3110 strain is genetically modified to express GFP, the RP437 strain has a plasmid. This plasmid gives the bacterium resistance to an antibiotic, CAM in this case, which permits to select fluorescent bacteria. The growth medium is also different than in Chapter 2, instead of a rich medium as LB, the culture was grown in M9G, which is a minimal medium that controls prototypic expression but allows cell division, and then the phosphate motility buffer used after centrifugation, is similar to the MMA used in Chapter 2. Finally, in this experiment large amount of bacterial suspension is needed (100 µL here versus 1 µL in Chapter 2), which makes necessary to centrifuge twice the bacteria. Every time a bacterial suspension is centrifuged, bacteria may lose activity, so to prevent that, the centrifugation here was slower and less time that in Chapter 2.